Flow, Turbulence and Combustion (2026) 116:58
https://doi.org/10.1007/s10494-026-00749-9

REVIEW

EMD Analysis of the Flow Field in an Internal Combustion Engine

Tim Wegmann[1] · Esther Lagemann[2] · Matthias Meinke[1] · Wolfgang Schröder[1,3]

Received: 23 December 2025 / Revised: 13 April 2026 / Accepted: 14 April 2026 /
Published online: 26 May 2026

Abstract

One of the major problems of the investigation of the flow field in internal combustion engines is the analysis of the impact of cyclic variations on the overall flow structure. Implicit large-eddy simulations (LES) are conducted to quantitatively analyze cold in-cylinder flow with associated cyclic variations in an internal combustion engine. To validate the simulation results, a comparison with stereoscopic PIV measurements in the tumble plane is performed and a grid convergence study is conducted in which five consecutive engine cycles are simulated using meshes ranging from 4.2 to 212 million cells. To quantitatively assess the agreement with the experimental data, weighted relevance and magnitude indices are evaluated for the instantaneous and ensemble averaged velocity vector during the intake and compression strokes. The influence of the number of simulated intake and compression cycles on the results is assessed. The grid convergence study demonstrates that the tumble spin and breakup processes are not accurately resolved by the coarse mesh, although the single-grid estimator suggests sufficient mesh resolution. Overall, satisfactory agreement with experimental data is achieved with sufficient mesh resolution. To analyze cyclic variations, a 2-D noise-assisted multivariate EMD method is applied to the experimental and numerical results. A novel mode separation of the velocity scales, which utilizes the identical decomposition of the ensemble averaged and instantaneous cycle data, is presented. This method simplifies the extraction of the tumble vortex core, enables the estimation of the ensemble mean flow and the analysis of cycle-to-cycle variations despite the limited number of available simulation cycles. The EMD analysis reveals a significant cyclic variance in the position of the tumble vortex core at crank angles between 90 to 120 degrees and 180 to 200 degrees. A correlation between the vortex core position and vortex strength at top dead center is established.

Keywords Large-eddy simulation · In-cylinder flow · Empirical mode decomposition · Tumble vortex · Single-grid estimator

Extended author information available on the last page of the article

1 Introduction

The accurate prediction of the flow in an internal combustion engine during the intake and compression stroke still is a challenging problem. In the temporally varying domain with opening and closing valves, the intake jets with small scale turbulent structures generate the larger scale vortical tumble motion which breaks down in the later stage of the compression stroke. The small scale turbulence as well as the large scale motion have an important impact on the fuel mixing (Wegmann et al. 2023) and the correct prediction of the combustion process (Engelmann et al. 2023). Therefore, engine efficiency and pollutant emission predictions require a sufficiently accurate simulation of the flow field during intake and compression. Since the initial condition of each intake and compression cycle is defined by the flow field at the end of the previous cycle, cycle-to-cycle variations (CCV) occur, which have to be known to achieve a robust engine performance.

Large-eddy simulations (LES) have become an important numerical approach for the analysis of in-cylinder flows. Due to the complexity of the flow field, challenges in the formulation of accurate boundary conditions, and generation meshes with sufficient resolution, numerical solutions must be validated. A comparison with experimental measurements allows the evaluation of the modeling assumptions and the errors from the numerical formulation. In LES, the modeling error of the sub-grid turbulent scales is directly connected with to the discretization error and the mesh resolution. With decreasing cell size, the discretization error is reduced and LES results converge towards direct numerical simulation (DNS) results. Consequently, numerical setups with different mesh resolutions are usually considered to obtain an estimate of the modelling error. To capture trends in the error estimate correctly the grid resolution must be varied considerably. In the present grid convergence study, cell lengths are bisected for the three different resolution cases, yielding mesh sizes between 4.2 to 212 million cells and mesh resolutions up to $1.06 \cdot 10^{-4}$ [m]. In this context, the single-grid estimator is discussed. This combination of validation and detailed grid convergence study is rare in the literature and reveals the limitations of the single-grid estimator.

Particle-image velocimetry (PIV) measurements have emerged as the dominant optical measurement technique for in-cylinder investigations (Baum et al. 2014). High-speed PIV measurements allow for the collection of the velocity data, typically in a limited field of view (FOV) at a high sampling rate. Hence, a collection of crank angle resolved data for hundreds of cycles is only restricted by data storage and camera processing speed. Many numerical studies rely on mono PIV measurements for validation, in which only in-plane velocity components are measured in a thin laser sheet (Barbato et al. 2023; Baumann et al. 2014; Krastev et al. 2019; Fang et al. 2022; Zhao et al. 2019). On the other hand, stereoscopic PIV measurements can measure all three velocity components throughout the intake and compression stroke. Such high-speed stereoscopic PIV measurements in the tumble plane of a 4-valve optical test engine operating at 1500 [RPM] are used to validate the numerical method. The difficulties associated with accurate boundary condition formulations, flow field validation, and assessment of the discretization error are addressed. A quantitative comparison between the LES results and the PIV measurements is discussed based on velocity comparative indices such as the weighted magnitude and relevance indices introduced by Willman et al. (2020). Furthermore, the tumble flow is analyzed in detail and the influence of the number of cycles on the ensemble mean data is addressed.

A two-dimensional multivariate empirical mode decomposition (EMD) methodology is applied to the numerical and experimental data in the experimental FOV at individual crank angles. This approach ensures the identical decomposition of the velocity input data and enables the comparison of the different intrinsic mode functions (IMFs) and the residual of mode components, i.e., the length scales. The numerical input data includes the instantaneous and ensemble averaged velocities, such that cycle-to-cycle variations can be determined. Unlike previous EMD analyses for in-cylinder flow applications (Sadeghi et al. 2021; Ding et al. 2023), a bidimensional formulation is applied. Both spatial directions are considered without the assumption of superposition. Additionally, a novel separation of IMFs in low and high frequency components is suggested. The proposed scale separation compares the energy of the extracted modes of the instantaneous and ensemble averaged input data such that it is independent from the number of extractable IMFs. This method enables the analysis of cycle-to-cycle variations despite the limited number of available simulation cycle data.

Typically, simulations of the flow field in internal combustion engines require a larger number of cycles to obtain the converged ensemble averaged velocity or to analyze cycle-to-cycle variations. Different numbers of cycles are reported in the literature, ranging from 10 to 50 (Engelmann et al. 2023; Barbato et al. 2023; Baumann et al. 2014; Krastev et al. 2019). With limited compute time this is feasible only for lower mesh resolutions. The presented novel approach ensures reliable separation of the velocity data into low and high frequency components. The low frequency component of the ensemble average velocity from only five cycles provided a good approximation of the converged ensemble average, while the low frequency velocity component of the individual cycles can be used to analyze cycle-to-cycle variations of the tumble motion. This allows the computation of ensemble averaged velocity field at high mesh resolutions from as few as five simulation cycles.

This paper is structured as follows. First, the governing equations and the numerical method are briefly summarized. Then, the engine setup with the applied boundary conditions is introduced. Subsequently, the simulation results are validated by PIV data and a grid and statistical data convergence study is presented. Then, the EMD methodology is presented and applied to separate the velocity field in low and high frequency components. The decomposition of the velocity field is evaluated and their relation to CCVs is shown. Finally, concluding remarks are given.

2 Mathematical Model

The motion of a compressible, viscous fluid is governed by the conservation equations for mass, momentum, and energy, i.e., the Navier-Stokes equations. The set of equations is formulated in non-dimensional form for a time varying domain $\Omega(t)$ as

$$\frac{d}{dt}\int_{V\ (t)} \mathbf{Q}\, dV + \oint_{\partial V\ (t)} (\underline{\mathbf{H}}^{\mathrm{inv}} + {}^{\mathrm{vis}}) \cdot \mathbf{n}\, d\Gamma = \mathbf{0}, \tag{1}$$

where $V(t) \subset \Omega(t)$ is a moving control volume bounded by the surface $\Gamma(t) = \partial V(t)$ with the outward pointing normal vector $\boldsymbol{n}$. The vector of conservative variables $\boldsymbol{Q} = [\rho, \rho\boldsymbol{u}, \rho E]^T$ contains the gas phase density ρ, velocity vector $\boldsymbol{u}$, and the total specific energy per unit mass E. The inviscid $\underline{\boldsymbol{H}}^{\mathrm{inv}}$ and viscous flux tensors $\underline{\boldsymbol{H}}^{\mathrm{vis}}$ in the arbitrary Lagrangian-Eulerian (ALE) formulation (Hirt et al. 1974) are given by

$$\underline{\boldsymbol{H}}^{\mathrm{inv}} + \underline{\boldsymbol{H}}^{\mathrm{vis}} = \begin{bmatrix} \rho(\boldsymbol{u} - \boldsymbol{u}_{\partial V}) \\ \rho\boldsymbol{u}(\boldsymbol{u} - \boldsymbol{u}_{\partial V}) + p\underline{\boldsymbol{I}} \\ \rho E(\boldsymbol{u} - \boldsymbol{u}_{\partial V}) + p\boldsymbol{u} \end{bmatrix} + \frac{1}{Re_0}\begin{bmatrix} 0 \\ \underline{\boldsymbol{\tau}} \\ \underline{\boldsymbol{\tau}}\boldsymbol{u} + \boldsymbol{q} \end{bmatrix} \tag{2}$$

with the pressure p, the velocity of the control volume surface $\boldsymbol{u}_{\partial V}$, and the unit tensor $\underline{\boldsymbol{I}}$. All equations are non-dimensionalized by reference values defined by the state at rest denoted by the index $(\cdot)_0$. Dimensional variables are denoted by $\overline{(\cdot)}$. The Reynolds number is based on the reference values $Re_0 = \frac{\overline{\rho_0}\,\overline{a_0}\,\overline{L_0}}{\overline{\mu_0}}$ using the speed of sound at rest $\overline{a_0} = \sqrt{\gamma\,\frac{\overline{p_0}}{\overline{\rho_0}}}$ with the heat capacity ratio of air $\gamma = 1.4$ and the characteristic length $\overline{L_0}$ which is the engine bore. Assuming a Newtonian fluid with zero bulk viscosity, the stress tensor $\underline{\boldsymbol{\tau}}$ reads

$$\underline{\boldsymbol{\tau}} = \frac{2}{3}\mu(T)\left(\nabla\cdot\boldsymbol{u}\right)\underline{\boldsymbol{I}} - \mu(T)\left(\nabla\boldsymbol{u} + (\nabla\boldsymbol{u})^T\right), \tag{3}$$

in which the dynamic viscosity $\mu(T)$ is determined by Sutherland's Law (Sutherland 1893)

$$\mu(T) = T^{3/2}\frac{1 + \overline{S}/\overline{T_0}}{T + \overline{S}/\overline{T_0}}. \tag{4}$$

The constant $\overline{S} = 111K$ is used for air at moderate temperatures (White 2006). The heat flux based on Fourier's Law with the Prandtl number for air $Pr_0 = 0.72$ reads

$$\boldsymbol{q} = -\frac{\mu(T)}{Pr_0(\gamma - 1)}\nabla T. \tag{5}$$

The equations are closed by the ideal gas law in non-dimensional form

$$\gamma p = \rho T\,. \tag{6}$$

The boundary of the fluid control volume $\Gamma(t) = \partial V(t)$ can be expressed as the zero contour of the signed-distance, i.e., level-set function $\varphi(\mathbf{x}, t)$. The combined level-set φ_0 can be constructed from all individual surface elements by

$$\varphi_0(\mathbf{x}, t) = \begin{cases} -\sqrt{\sum_{i=1}^{N}\varphi_i^2(\mathbf{x}, t)}, & \text{if all } \varphi_i(\mathbf{x}, t) < 0 \\ \min\left(\sum_{i=1}^{N}\varphi_i(\mathbf{x}, t)\right), & \text{otherwise.} \end{cases} \tag{7}$$

Each solid moving surface may evolve by an individual transport equation

$$\frac{\partial\varphi_i}{\partial t} + v_{\Gamma,i}(t)\cdot\nabla\varphi_i = 0 \quad , \tag{8}$$

with its translational motion $v_{\Gamma,i}(t)$.

2.1 Boundary Conditions

At solid moving walls a no-slip constraint is imposed as a Dirichlet-type boundary condition with the prescribed wall velocity $\mathbf{u}_{\Gamma,i}$. Walls are considered adiabatic with a Robin-type pressure boundary condition (Schneiders et al. 2013; Udaykumar et al. 2001)

$$\frac{\partial p}{\partial n} = -\left(\rho \frac{D\mathbf{u}}{Dt} \cdot \mathbf{n}\right) \quad , \forall \boldsymbol{x} \in \Gamma(t) \,. \tag{9}$$

Inflow and outflow are formulated as Navier-Stokes characteristic boundary conditions (NSCBC) (Poinsot and Lele 1992) to account for local and temporal flow reversal. A wave analysis of the local one-dimensional inviscid (LODI) Euler equations leads to the description of the time varying amplitude of the characteristic waves $\mathcal{L}$ in primitive variable formulation with

$$\mathcal{L} = \begin{pmatrix} (u-a)\left(\frac{\partial p}{\partial x} - \rho a \frac{\partial u}{\partial x}\right) \\ (u+a)\left(\frac{\partial p}{\partial x} + \rho a \frac{\partial u}{\partial x}\right) \\ u\frac{\partial v}{\partial x} \\ u\frac{\partial w}{\partial x} \\ u\left(a^2 \frac{\partial \rho}{\partial x} - \frac{\partial p}{\partial x}\right) \end{pmatrix} = \begin{pmatrix} \text{inward acoustic} \\ \text{outward acoustic} \\ \text{transversal} \\ \text{transversal} \\ \text{entropy} \end{pmatrix} . \tag{10}$$

The eigenvalues of the equation system are $\lambda = u + a, u - a, u, u, u$. The amplitude of waves exiting the fluid domain can be computed directly from the numerical solution. For waves entering the domain a generalized relaxation method as proposed in (Pirozzoli and Colonius 2013) is used to ensure convergence towards prescribed quasi steady state target values. The wave amplitudes are then multiplied by the eigenvector matrix of the equation system and converted in the conservative variable formulation.

3 Numerical Method

The numerical prediction of in-cylinder flow is conducted using two non-conforming and distinct solution methods. A finite-volume method (FV) is employed to solve the fluid conservation equation and a semi-Lagrange level-set solver (Günther et al. 2014) is utilized to determine the evolution of embedded moving boundaries, i.e., the independent motion of the engine piston and valve geometries. Due to different grid spacing requirements each solver uses an individual subset of the joint hierarchical grid, which is locally refined and adapted during the simulation. The domain decomposition is based on the Hilbert space-filling curve, which is applied to the joint hierarchical Cartesian grid and ensures efficient coupling without communication overhead. Due to the time varying computational domain and grid adaptation, the computational load varies significantly over time. To achieve high parallel efficiency, dynamic load balancing is employed based on a redistribution of the cells (Niemöller et al. 2020; Wegmann et al. 2025). The multi-physics solver m-AIA (2024) developed at the Institute of Aerodynamics at RWTH Aachen University is utilized. The framework has been applied previously to in-cylinder flow (Wegmann et al. 2023, 2024; Schneiders et al. 2013; Berger et al. 2020).

3.1 Finite-Volume Solver

The turbulent flow field is predicted using a large-eddy simulation (LES) with a cell-centered finite-volume method, in which a monotone integrated LES (MILES) approach is employed. In this formulation, large turbulent scales are resolved and the truncation of the numerical scheme acts as a subgrid scale model for scales smaller than the grid filter. The inviscid fluxes in the Navier-Stokes equations are approximated using a low-dissipation variant of the advection upstream splitting method (AUSM) as proposed in (Meinke et al. 2013). The viscous fluxes are approximated by a central-difference scheme, where gradients at the cell-surface centers are computed using the re-centering approach by Berger et al. (2012). Cell-centered gradients are calculated using a weighted least-squared reconstruction scheme ensuring that a second-order accurate scheme in space is obtained. Second-order accurate time integration is achieved by an explicit five-stage Runge-Kutta scheme for moving boundary problems. Runge-Kutta coefficients optimized for stability as proposed by Schneiders et al. (2016) are utilized. The time step Δt is computed based on the Courant-Friedrichs-Lewy (CFL) constraint. The immersed moving boundaries are represented by a conservative sharp multiple-cut-cell and split-cell method as described in (Schneiders et al. 2013). A multiple-ghost cell approach is used to prescribe the flow state individually for cut cells assigned to more than one boundary condition. A combined interpolation and flux-redistribution technique yields a conservative and stable numerical method for small cells. Further details on the overall numerical method can be found in (Günther et al. 2014; Schneiders et al. 2016; Pogorelov et al. 2018).

3.2 Level-Set Solver

The transport equation for individual level-set functions can be solved numerically to determine the temporal change of moving interfaces. Due to the accumulation of the numerical truncation error during the time integration, the accuracy of the moving geometries may deteriorate. A different approach can be employed for translational motion of solid interfaces, i.e., a spatially constant extension velocity, where the level-set is computed by interpolation of two reference level-set distributions. For this semi-Lagrange solver (Günther et al. 2014) the error of the geometric representation of the surface is reduced to a constant interpolation error.

For the in-cylinder flow application, each level-set function represents various parts of the engine, e.g., the cylinder head, piston, and valve geometry which may evolve independently. The distance from each surface can be used to determine the gap width between approaching interfaces, i.e., when valves are close to their valve seat. However, the flow solution can deteriorate significantly when gaps between boundary interfaces become significantly smaller than the local cell size. Therefore the combined level-set field in the vicinity of the gap is modified to an artificially closed gap (Günther et al. 2014). Since only the combined level-set is changed, no surface information is lost through this modification. The threshold width for the opening/closing procedure can be chosen arbitrarily and may be significantly smaller or larger than local cell lengths. Additionally, the closing and opening procedure of gaps can be enforced at specific time instances which is applied here for consistent gap treatment in the grid convergence study.

4 Setup

The flow field in a 4-valve direct injection research engine is simulated. First, a mesh refinement study is conducted and subsequently, 3 component PIV measurement data are used to validate the numerical method.

4.1 Experimental Setup

The flow in the research engine has been analyzed in extensive experimental studies in previous work. Braun et al. (2018) investigated how intake valve lift and timing affect the flow field in tumble and cross-tumble planes through PIV measurements. In (Braun et al. 2019), high-speed tomographic PIV measurements within a thin volume around the tumble plane were compared with stereoscopic PIV measurements. Recently, high-speed stereoscopic PIV measurements with improved spatial and temporal resolution in the tumble plane were presented in (Braun et al. 2020). These high-resolution stereoscopic PIV data were utilized for the validation of the numerical method and the analysis of CCVs in this paper.

For the PIV measurements a supercharge is used to adjust the static pressure at the intake manifold to 1.0 [bar]. Furthermore, an intake temperature of approx. 23.0 [°C] is reported in (Braun et al. 2018). A high-speed dual-cavity PIV laser with a wavelength of 527 [nm] is used with a pulse separation of 20 [μs] and a frequency of 2000 [Hz] per cavity. The flow is seeded with DEHS particles with a mean particle diameter in the range of $0.35 - 0.45 \mu m$. With the Stokes number of the particles estimated to $St \approx 0.0018$ (Braun et al. 2020), the flow tracing error is below 1% (Tropea et al. 2007). To capture the three-dimensional particle motion, two cameras equipped with Tamron 180 [mm] macro lenses and an aperture of f/5.6 are arranged at an angle of $\pm 45°$ relative to the normal of the tumble plane.

The research engine, designed with enhanced optical access, features a flat glass piston equipped with dual piston rings that have been shifted downward along the bore axis to facilitate lateral optical access into the cylinder. This approach is commonly used in optical test engines (Baumann et al. 2014; Braun et al. 2018; Janas et al. 2017). It reduces the piston sealing and increases the effective clearance and crevice volume of the motored engine. As a result, a significant reduction in the effective compression rate is observed in the experimental test engine. Various methods have been proposed to achieve matching compression ratios in numerical setups. In (Fang et al. 2022), the crevice length of the engine geometry in the simulation is modified until the experimental peak pressure is matched. Another approach involves adjusting the intake pressure and mass flux according to experimental pressure measurements taken at the intake port for a specific engine and operational condition. Furthermore, a porous boundary condition can be implemented at the piston-liner intersection to simulate the blow-by effect in the optical test engine, which is significantly lower in real engines due to gap sealing by the oil film layer. The numerical blow-by mass flux is based on empirical relations and has to be fine-tuned to match the experimental peak pressure curve (Zhao and Lee 2006; Namazian and Heywood 1982). Note that such modifications of boundary conditions or geometric changes are usually only valid for a specific test engine and specific operation conditions. Janas et al. (2017), however, suggest that the influence of the predicted peak pressure might not be as relevant under motored conditions as under fired conditions. The objective of this work is to create a validated numerical framework for the simulation of non-optical engine geometries, various operational conditions and direct injection configurations, for which the engine peak pressure or other parameters may not be available. Consequently, tuning the simulation parameters to match the specific peak pressure of the optical engine is not performed. Instead, a general formulation based on non-reflecting boundary conditions is employed, which only requires the definition quantities at rest. This approach results in a peak pressure that differs from that of the optical test engine, since perfect piston sealing is assumed in the numerical setup. The effective compression ratio is 8.4 for the numerical setup and 5.4 for the experimental optical test bench.

4.2 Numerical Setup

For the formulation of the non-reflecting in- and outflow conditions at the intake and exhaust port, the intake port duct is extended 2.5 bore diameters upstream, while the exhaust port is extended 1.9 diameters downstream. These extensions are implemented to ensure that the main flow direction is parallel to the duct axis. All relevant engine geometry and motored operating parameters are summarized in Table 1.

The standard valve timing is summarized in Table 1 and shown in Fig. 1, where opening and closing timings are specified in crank angles corresponding to a valve lift of 0.001 [m]. The experimental valve lift curves are obtained from measurements by Braun et al. (2018). The valve lift curves are approximated numerically by a shifted sine function and the motored piston position at crank angle Θ is given by the piston motion equation with the stroke and rod lengths l_s and l_r.

At the intake and exhaust ports Navier-Stokes characteristic boundary conditions are imposed using the generalized relaxation method from (Pirozzoli and Colonius 2013). In this formulation, the NSCBC define a temporal change of the conservative variables, which is used in the Runge-Kutta time stepping method to impose the boundary conditions. The set of unsteady target values for the pressure and temperature (p_t, T_t) can be determined by assuming an isentropic expansion from a stagnation reference state (T_{ref}, p_{ref}) to the spatially averaged Mach number at the intake and exhaust. At the intake port, the flow is assumed to be aligned with the port axis, i.e., the transversal target velocities (v_t, w_t) are set to zero, and the flow is assumed to be free of turbulent fluctuations. The normal velocity in the first inner cell at the port determines whether there is an in- or outflow state. This determines how many characteristic wave amplitudes must be prescribed, i.e., for the outflow

Table 1 Optical test engine parameters

Parameter	Value [Unit]
Nominal compression ratio	7.4:1 [-]
Bore (L_{ref})	0.075 [m]
Stroke length (l_s)	0.0825 [m]
Connecting rod length (l_r)	0.146 [m]
Valve lift	0.009 [m]
Exhaust valve open	564 [CAD]
Exhaust valve close	20 [CAD]
Intake valve open	708 [CAD]
Intake valve close (IVC)	196 [CAD]
Intake temperature (T_{ref})	23.0 [°C]
Intake pressure (p_{ref})	1.0 [bar]
Engine speed (RPM)	1500 [1/ min]
Average piston velocity (u_p)	4.125 [m/s]

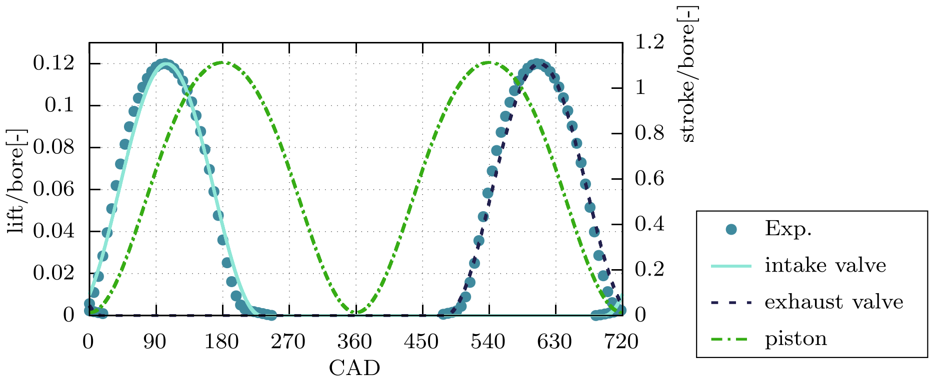

Fig. 1 Temporal evolution of the valve and piston position as a function of the crank angle (CAD) after top dead center of the gas exchange (aTDC). Symbols represent the experimental valve lift measurements from (Braun et al. 2018)

state only $\mathcal{L}_1$ needs to be prescribed, whereas $\mathcal{L}_{2,3,4,5}$ need to be prescribed for the inflow state. The resulting characteristic wave amplitudes are determined by

$$\mathcal{L} = \begin{pmatrix} \sigma_1 \frac{a\left(1-Ma_{\max}^2\right)}{L_x}\,(p-p_t) \\ \sigma_2 \frac{a\left(1-Ma_{\max}^2\right)}{L_x}\,(p-p_t) \\ \sigma_3 \frac{a}{L_x}\,(v-v_t) \\ \sigma_4 \frac{a}{L_x}\,(w-w_t) \\ \sigma_5 \frac{\rho a}{L_x}\,(T-T_t) \end{pmatrix}, \tag{11}$$

where L_x is a characteristic length, $Ma_{\max}$ the maximum Mach number at the boundary, and σ_i is a relaxation parameter controlling the non-reflecting property of the boundary and the well-posedness of the problem. Selle et al. (2004) suggest values in the range of $0.2 < \sigma_{1,2} < \pi$ for one-dimensional duct flow using the duct length as characteristic length L_x. A value of $\sigma_{1,2} = 1.7$ is used and the characteristic lengths L_x is set to the length of the intake and exhaust port, respectively. All other σ values are set to 0.28 corresponding to 'optimal' non-reflecting behavior as proposed in (Poinsot and Lele 1992; Rudy and Strikwerda 1980). These in- and outflow conditions allow local and global flow reversals, which occurs, e.g., at the intake port at the end of the intake stroke.

As mentioned before, the boundary conditions from the experiment are not imposed directly, e.g., in form of a time resolved intake port pressure obtained from measurements. The formulation in the numerical solution is based on stagnation point values and is general in the sense that it does not involve parameter tuning or any iterative procedure such that it can be applied directly to various engine setups and operating conditions. A more detailed discussion of the suitability of the intake port boundary condition is provided in the appendix.

For the grid refinement study, large-eddy simulations are performed for three meshes using solution adaptive and boundary mesh refinement as shown in Fig. 2. Each mesh is generated using the same uniform base mesh level, which is refined locally by successive bisection of the cell length. For the *coarse* mesh the largest and smallest cell lengths are

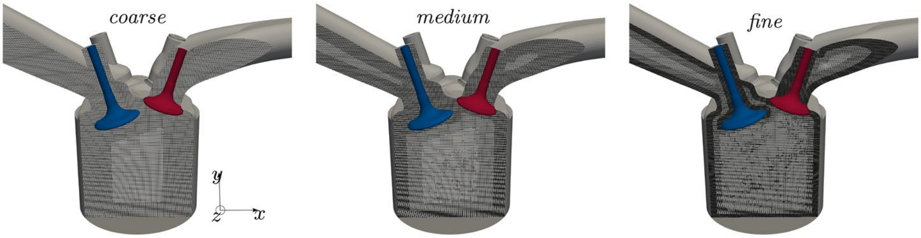

Fig. 2 Geometry of the direct injection research engine visualized by the front intake and exhaust valves. The solution adaptive Cartesian mesh is shown at the intake valve plane at 110 crank angle degree (CAD) after top-dead center for a *coarse*, *medium*, and *fine* resolution. The x-axis of the coordinate system is oriented towards the exhaust pipe and the y-axis is aligned with the engine bore

Table 2 Spatial steps and computational resources for the coarse, medium and fine mesh

Mesh resolution	coarse	medium	fine
Smallest cell length [m]	$4.27 \cdot 10^{-4}$	$2.13 \cdot 10^{-4}$	$1.06 \cdot 10^{-4}$
Largest cell length [m]	$1.71 \cdot 10^{-3}$	$8.53 \cdot 10^{-4}$	$4.27 \cdot 10^{-4}$
No. of active FV cells [$1 \cdot 10^6$]	4.2–7.5	27.5 - 41.7	146 - 212
No. of time steps per cycle[$1 \cdot 10^3$]	94	169	403
Disk space per cycle [TB]	≈ 0.15	≈ 0.61	≈ 3.0

$1.71.10^{-3}$ and $4.27 \cdot 10^{-4}$ [m]. The next finer, i.e., medium, mesh resolution uses half of these values for the smallest and largest cells. Since the local mesh resolution is controlled by solution adaptive mesh refinement using flow sensors, not all mesh cells of the coarser mesh are refined for the medium mesh. The resulting cell length ranges for the *coarse*, *medium* and *fine* setups are summarized in Table 2. For the finest mesh, the smallest cell length is approx. 106 [μm]. The significant increase in computational cost and disk space requirements with increasing resolution is evident from Table 2. Computing a single cycle using the *medium* grid resolution is approx. 10.8 times more expensive than the *coarse* mesh due the increase in cells by a factor of six and a reduction in the time step by a factor of 1.8. The time step is defined by a constant CFL-number of $CFL = 0.95$, which corresponds to a time step of approx. $1.9 \cdot 10^{-7}$ [s] for the *fine* mesh.

The solution adaptive boundary refinement ensures that the solid surfaces, i.e., the moving valves, piston, and engine liner, are resolved with the smallest cells. A smooth transition of the mesh resolution towards the coarser base level is achieved using a region-growing algorithm. The flow field is further refined locally by one mesh level based on the maximum magnitude of the velocity gradient $(\max(|\nabla \boldsymbol{u}|))$. The minimum and maximum threshold values, which are based on the statistical distribution of the sensor field, control the solution adaptive mesh refinement.

The simulations start at top dead center (TDC) before the first intake stroke with quiescent flow as an initial condition. For the *finest* mesh six consecutive cycles and for the *coarse* and *medium* mesh cases 11 cycles are computed. In all cases, the first cycle is disregarded for the postprocessing of the results.

5 Flow Field Quantities

In the experimental setup, the stereoscopic particle-image velocimetry (PIV) is conducted with a spatial resolution of approximately 0.00056 [m] or 0.0075 times the bore length. Double images, separated by a time difference of 20 [μs], are recorded every 4.5 [CAD] in the crank angle range of 45–315 during the intake and compression stroke in the central tumble plane of the engine, i.e., at $z = 0$. The experimental FOV is shown in Fig. 4. All velocities are non-dimensionalized by the average piston velocity $u_p = \frac{\mathrm{RPM}\cdot l_s}{30}$ [m/s].

During the numerical simulation, snapshots of the entire in-cylinder flow field are stored at intervals of 5 [CAD] and the tumble plane data are extracted additionally at every crank angle. The mesh resolution for a given crank angle can differ for individual cycles due to the solution dependent adaptive mesh refinement. Therefore, the flow field data are interpolated to a reference grid to compute ensemble averages (EA) from multiple cycles in a post-processing step. Note that this interpolation in the post-processing has no influence on the solution procedure.

To compare the experimental and numerical data, the LES results are linearly interpolated to the data points in the experimental FOV and to the same crank angle intervals. This is done to minimize deviations caused by different temporal and spatial filtering operations (Barbato et al. 2023; Krastev et al. 2019).

In the following, $\widetilde{\Psi}$ is used to denote the integration of any quantity Ψ over the entire engine volume $V(t)$. If the additional subscript $\widetilde{\Psi}_E$ is added, the integration is only performed over the experimental FOV in the tumble plane.

The turbulent flow field is characterized by the instantaneous specific kinetic energy $e(t)$, which can be integrated over the volume $V(t)$ at a specific time t

$$\widetilde{e}(t) = \frac{1}{2\,V(t)} \oint_{V(t)} \left(u(\boldsymbol{x},t)^2 + v(\boldsymbol{x},t)^2 + w(\boldsymbol{x},t)^2 \right) dV. \tag{12}$$

The time t can be associated to a certain cycle i and crank angle $0 \le \theta_i \le 720°$ such that any quantity can be expressed as $\Psi(t) = \Psi(\theta_i)$. Variations in the integral values between the cycles i indicate cycle-to-cycle variations (CCV).

The volume average of the z-component of the vorticity Ω in the mathematical positive direction of rotation is computed by

$$\widetilde{\Omega}(t) = \frac{-1}{V(t)} \oint_{V(t)} \left(\frac{\partial v(\boldsymbol{x},t)}{\partial x} - \frac{\partial u(\boldsymbol{x},t)}{\partial y} \right) dV. \qquad \text{(Cite Figure.13)}$$

Positive values of $\widetilde{\Omega}$ indicate a large scale circular motion around the z-axis, which is commonly referred to as the tumble ratio (TR) (Huang et al. 2005) and the coherent motion as the tumble vortex. The vorticity is non-dimensionalized by the angular velocity of the crank shaft, i.e., $2\pi\,\frac{\mathrm{RPM}}{60}$.

Following the Reynolds decomposition, the instantaneous flow field can be separated into an ensemble averaged $\langle\Psi\rangle$ and a fluctuating component $\Psi\prime_i$ for all crank angles θ

$$\langle \Psi(\boldsymbol{x},\theta) \rangle = \frac{1}{N} \sum_{i=0}^{N-1} \Psi(\boldsymbol{x},\theta_i) \quad \text{and} \tag{14}$$

$$\Psi'(\boldsymbol{x},\theta_i) = \Psi(\boldsymbol{x},\theta_i) - \langle\Psi(\boldsymbol{x},\theta)\rangle, \qquad \text{(Cite Figure.15)}$$

where the index i denotes a specific cycle and N the number of cycles included in the averaging. The cycle average of $\langle\Psi\rangle$ is reduced to $\Psi(\theta, N)$, independent of i.

In this formulation, the fluctuating components contain both turbulent and cycle-to-cycle variations. Based on the decomposition of the velocity, the specific kinetic energy of the fluctuation $k(\boldsymbol{x},\theta)$ and the kinetic energy of the mean velocity field $K(\boldsymbol{x},\theta)$ are defined as

$$k(\boldsymbol{x},\theta) = \frac{1}{2}\frac{1}{N}\sum_{i=0}^{N-1}\left(u\prime^2(\boldsymbol{x},\theta_i) + v\prime^2(\boldsymbol{x},\theta_i) + w\prime^2(\boldsymbol{x},\theta_i)\right), \tag{16}$$

$$K(\boldsymbol{x},\theta) = \frac{1}{2}\left(\langle u\rangle^2(\boldsymbol{x},\theta) + \langle v\rangle^2(\boldsymbol{x},\theta) + \langle v\rangle^2(\boldsymbol{x},\theta)\right). \tag{17}$$

Note that k contains turbulent and cycle variations and therefore, it differs from the turbulent kinetic energy in turbulence modeling formulations such as RANS.

To identify the vortex core of the large scale tumble motion, the vortex tracking algorithm proposed by Graftieaux et al. (2001) is employed. This method has been applied to in-cylinder flow fields in previous studies (Braun et al. 2018; Zentgraf et al. 2016; Falkenstein et al. 2017; Stiehl et al. 2016. The vortex identification function Γ is defined at a point $\boldsymbol{x}$ located in a plane as

$$\Gamma(\boldsymbol{x}) = \frac{1}{S}\sum_{j=1}^{S}\frac{\boldsymbol{r}_j \times \boldsymbol{v}_j}{|\boldsymbol{r}_j|\,|\boldsymbol{v}_j|} \quad , \tag{18}$$

using the distance r_j and relative velocity vector $\boldsymbol{v}_j$ between the point $\boldsymbol{x}$ and the neighbor j. S in-plane points, which are usually the mesh or measurement points around the location $\boldsymbol{x}$ are considered. Values of the scalar vortex identification function range within $\Gamma \in [-1, 1]$, where a threshold value of $|\Gamma|$ between 0.65 and 0.8 is typically used to detect the vortex core (Janas et al. 2017; Falkenstein et al. 2017). The value obtained for Γ depends on the number of neighboring points S used in Eq. 18 and the local velocity scales in the associated area. Braun et al. (2018) used $S = 8$ neighboring points, whereas Zentraf et al. (2016) used a larger area including 80 points, while Stiehl et al. (2016) used all measurement points in the plane.

When comparing results from numerical simulations using different mesh resolutions, it is not meaningful to just use a fixed number of direct neighboring mesh cells since this yields different areas for which the vortex identification function is computed such that the result will depend on the chosen grid resolution. Instead, it is more meaningful to define the area based on a reference length. Falkenstein et al. (2017) suggest an area size with a diameter which corresponds to $1/4$ of the bore length. Note that the vortex core is smeared out between neighboring cells with increasing area size. Additionally, the computational cost for the determination of Γ increases significantly. On the other hand a small area with only a few neighboring points on can lead to an erroneous identification of smaller turbulent vortex cores instead of the large scale tumble vortex. This problem mainly occurs with LES results using higher mesh resolution, while it does not exist for RANS solutions or in the ensemble averaged flow field of the PIV measurements. In the current study the detection of a single tumble vortex core position was found to work well for an area defined by a diameter of $1/4$ of the bore length with a threshold of 98% of the in-plane minimum value $\Gamma_{\min}$. More details about the vortex core identification using the instantaneous, highly resolved flow fields from the LES are included in the appendix.

A quantitative comparison between the PIV measurements and the numerical results is performed by the Relevance Index (RI), also known as Alignment Parameter, and the Magnitude Index (MI), also denoted Magnitude Similarity Index (Zhao et al. 2019; Willman et al. 2020; Liu and Haworth 2011; Buhl et al. 2017). The RI of two velocity fields $\boldsymbol{u}_A$ and $\boldsymbol{u}_B$ is defined

$$RI(\boldsymbol{x}) = \frac{\boldsymbol{u}_A(\boldsymbol{x}) \cdot \boldsymbol{u}_B(\boldsymbol{x})}{|\boldsymbol{u}_A(\boldsymbol{x})|\,|\boldsymbol{u}_B(\boldsymbol{x})|}, \tag{19}$$

containing the vector dot products and magnitudes of the velocities $|\boldsymbol{u}_A|$ and $|\boldsymbol{u}_B|$. RI becomes independent of the velocity magnitude due to the normalization. The value 1 expresses perfect alignment, while $RI = 0$ or $RI = -1$ show an orthogonal or opposite orientation.

The comparison is complemented by the MI, which depends on both magnitude and direction of the velocity vectors

$$MI(\boldsymbol{x}) = 1 - \frac{|\boldsymbol{u}_A(\boldsymbol{x}) - \boldsymbol{u}_B(\boldsymbol{x})|}{|\boldsymbol{u}_A(\boldsymbol{x})| + |\boldsymbol{u}_B(\boldsymbol{x})|}. \tag{20}$$

MI values lie between 0 and 1, where larger values correspond to a better alignment and identical magnitude. For the quantitative comparison RI and MI values are integrated over all data points of the experimental FOV.

Other studies have already shown that both integral indices can be sensitive to regions with low velocity magnitude, i.e., near the tumble vortex core (Krastev et al. 2019; Willman et al. 2020). Poor vector alignment in these regions is over-represented and can influence the integral values significantly. This is also true for the presented findings and is confirmed in the appendix. Consequently, an additional weighting based on the local velocities $\boldsymbol{u}_A$ and $\boldsymbol{u}_B$ has been suggested. Different weighting functions were introduced, e.g., based on the velocity magnitudes (Willman et al. 2020) or the kinetic energy (Krastev et al. 2019). The velocity weighted indices WMI and WRI introduced by Willman et al. (2020) are applied in this study

$$WRI(\boldsymbol{x}) = \frac{1 - RI(\boldsymbol{x})}{2} \frac{|\boldsymbol{u}_A(\boldsymbol{x})|}{\mathrm{median}\,(|\boldsymbol{u}_A|)} \frac{|\boldsymbol{u}_B(\boldsymbol{x})|}{\mathrm{median}\,(|\boldsymbol{u}_B|)} \tag{21}$$

$$WMI(\boldsymbol{x}) = \frac{||\boldsymbol{u}_A(\boldsymbol{x})| - |\boldsymbol{u}_B(\boldsymbol{x})|}{\mathrm{median}\,(|\boldsymbol{u}_A|, |\boldsymbol{u}_B|)}. \tag{22}$$

The median of the velocity magnitude field is used to provide a robust non-dimensionalization (Willman et al. 2020). Note that the formulation of the weighted magnitude index only considers the magnitude of the velocity fields. Therefore, it differs from the MI formulation. WRI and WMI values of zero indicate a perfect match in alignment and magnitude. For a poor agreement no distinct maximum exists as the values depend on the distribution and mean of the velocity field data.

The strain rate tensor $\underline{\boldsymbol{S}}$ of the velocity field is evaluated for the different numerical set-ups. The instantaneous strain rate tensor entities $S_{i,j}$ at position $\boldsymbol{x}$ are given by

$$S_{i,j} = \frac{1}{2}\left(\frac{\partial u_i}{\partial x_j} + \frac{\partial u_j}{\partial x_i}\right). \tag{23}$$

The ensemble mean of the strain rate entities are computed as $\langle S_{i,j}\rangle$ and the scalar strain rate $\mathcal{S}$ is defined as

$$\mathcal{S} = \sqrt{2S_{i,j}S_{i,j}}, \tag{24}$$

where $\mathcal{S}$ corresponds to the Euclidian norm of the strain rate tensor. The Euclidian norm of the ensemble mean of the strain rate entities $||\langle S_{i,j}\rangle||$ is used to estimate the mean kinetic energy k_{SGS} of the unresolved sub-grid scales based on Smagorinsky's turbulence model (Smagorinsky 1963)

$$k_{SGS} = 2C_i\Delta^2||\langle S_{i,j}\rangle||^2 \quad , \tag{25}$$

with the filter width Δ as the local mesh cell length and the model constant $C_i = 0.202$. The modeling assumption can be used to define a single-grid estimator $M(\boldsymbol{x}, \theta)$ to evaluate the quality of the LES grid resolution (Barbato et al. 2023)

$$M = \frac{k}{k + k_{SGS}} = \frac{k}{k + 2C_i\Delta^2||\langle S_{i,j}\rangle||^2}. \tag{26}$$

The mesh resolution for the LES is considered *sufficient* if $M(\boldsymbol{x}, \theta) > 0.8$ meaning that presumably 80% of the turbulent structures are resolved (Barbato et al. 2023; Pope 2000). The suitability of this mesh quality index for in-cylinder flow will be discussed based on the grid convergence study in the following single-grid estimator section.

The velocity fluctuations $\boldsymbol{u\prime}$ are further analyzed by the determination of the fluctuating stress tensor ($\underline{\tau\prime}$) and the anisotropic invariant map (Lumley triangle) (Choi and Lumley 2001; Lumley 1978). The fluctuating stress tensor is given by

$$\underline{\tau\prime}(\boldsymbol{x})_{i,j} = \frac{\langle (u\prime_i u\prime_j)\rangle}{\langle (u\prime_k u\prime_k)\rangle} - \frac{1}{3}\underline{I} \tag{27}$$

and contains of both cycle-to-cycle and turbulent fluctuations. The Lumley triangle is characterized by the second (I_2) and third (I_3) invariant of the stress tensor given as

$$I_2 = -\frac{\tau'_{i,j}\tau'_{i,j}}{2} \quad I_3 = \frac{\tau'_{i,j}\tau'_{j,k}\tau'_{i,k}}{3}. \tag{28}$$

The resulting invariant map in Fig. 3 highlights different regions, which are used to characterize the turbulent state.

The Pearson correlation coefficient

$$r_{\Psi,\xi} = \frac{\sum_i^N \left(\Psi_i - \langle\Psi\rangle\right)\left(\xi_i - \langle\xi\rangle\right)}{\sqrt{\sum_i^N \left(\Psi_i - \langle\Psi\rangle\right)^2 \sum_i^N \left(\xi_i - \langle\xi\rangle\right)^2}} \tag{29}$$

is used to investigate the linear correlation between the data Ψ and ξ. Values of the Pearson correlation coefficient range between $\in [-1, 1]$ and the magnitude of r indicates the strength of the linear correlation, where 1 shows perfect linear behavior and 0 no linear connection. The sign of r indicates a direct or inverse correlation.

In general, in-cylinder research aims to obtain a triple decomposition of the flow quantity Ψ by

$$\Psi(\boldsymbol{x}, \theta_i) = \langle\Psi(\boldsymbol{x}, \theta)\rangle + \Psi(\boldsymbol{x}, \theta_i)'_{CCV} + \Psi(\boldsymbol{x}, \theta_i)'_{turb} \tag{30}$$

introduced by Heywood et al. (2018). Typically, this is applied to the velocity decomposition, where $\boldsymbol{u\prime}_{CCV}$ denotes large length scale fluctuations and $\boldsymbol{u\prime}_{turb}$ smaller turbulent fluctuations. Additionally, the Reynolds decomposition as introduced in Eq. 15) can be applied

$$\Psi(\boldsymbol{x}, \theta_i) = \langle\Psi(\boldsymbol{x}, \theta)\rangle + \Psi'(\boldsymbol{x}, \theta_i). \tag{31}$$

As mentioned before, the fluctuation part does not distinguish between CCV and turbulent fluctuations. To separate the fluctuations between larger and smaller length scales, different methods such as fast Fourier transform (FFT), proper orthogonal decomposition (POD) (Fogleman et al. 2004; Chen et al. 2012), or dynamic mode decomposition (DMD) (Sakowitz et al. 2014) have been applied. However, these methods either require a statistical convergence of the flow quantities or depend on a priori defined basis functions. Moreover, they cannot fully capture the unsteady and non-linear characteristics of turbulent flows.

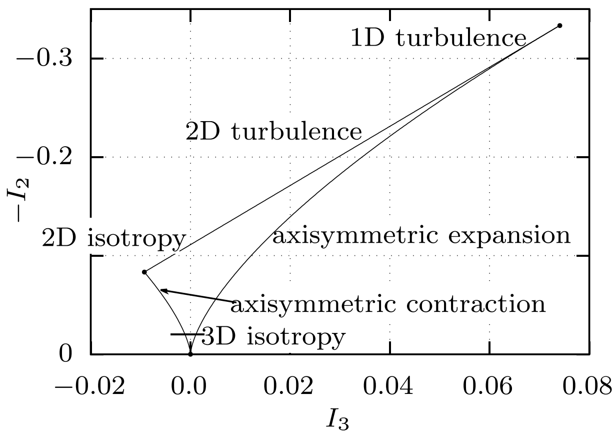

Fig. 3 Anisotropic invariant map (Lumley triangle) (Choi and Lumley 2001)

5.1 Empirical Mode Decomposition

Empirical mode decomposition (EMD) introduced by Huang et al. (1998) enables a data driven decomposition of unsteady, three-dimensional data into a series of intrinsic mode functions (IMFs). IMFs include amplitude and frequency modulation. The decomposition neither requires additional input parameters nor converged cycle statistics, since the Hilbert spectral analysis can identify instantaneous frequencies without requiring the data to include full wave lengths.

The decomposition involves an iterative 'sifting' process, in which individual modes with characteristic temporal or spatial scales are extracted from the data. In a first step, local extrema of the input data are detected and used to define an upper and lower envelope/spline function. The mean of these two envelopes is subtracted from the input data and the process is repeated until a stopping criterion is satisfied. At the end of each sifting iteration, the subtraction of the last mean envelope from the input data yields the new IMF and the remaining part is denoted as the residual. The residual is treated as input in the next sifting iteration until no further IMFs can be extracted. Thus, the first IMF contains the smallest scales, i.e., associated with the highest spatial wave number. With increasing mode number larger length scales are extracted.

Sadeghi et al. (2021) introduced EMD to the instantaneous in-cylinder velocity field obtained from PIV measurements and proposed a scale separation into low frequency (LF) and high frequency (HF) components as a combination of multiple IMFs

$$\Psi(\boldsymbol{x}, \theta_i) = \Psi(\boldsymbol{x}, \theta_i)_{LF} + \Psi(\boldsymbol{x}, \theta_i)_{HF}. \tag{32}$$

For the sake of consistency, their frequency terminology (LF and HF) is adopted, even though the extracted scales are length scales and not temporal scales.

In Sadeghi et al. (2021) only the residual is considered as the LF part, whereas Ding et al. (2023) use a combination of the last IMF and the residual. However, the number of extractable IMFs depends on the characteristics of the EMD input data such as spatial resolution and FOV. Therefore, a novel separation into LF and HF parts based on the energy of the extracted modes is proposed and will be presented in the following. It should be noted that the remaining residual does not necessarily fulfill IMF properties (Huang et al. 1998).

A two-dimensional multivariate EMD (MEMD) is applied simultaneously to the velocity field of the instantaneous and ensemble averages numerical solution and the ensemble averaged PIV data. This means that the mode decomposition and scale separation is simultaneously applied to the ensemble averaged data

$$\langle \Psi(\boldsymbol{x}, \theta) \rangle = \langle \Psi(\boldsymbol{x}, \theta) \rangle_{LF} + \langle \Psi(\boldsymbol{x}, \theta) \rangle_{HF}. \tag{33}$$

This procedure ensures the identical decomposition of the different input data allowing for a comparison between the LF and HF components of the individual cycles, the ensemble average and between numerical and experimental results. Since the MEMD input data contain cycle-to-cycle fluctuations and mean components, additional physically meaningful information is incorporated in the input.

A noise assisted extension is employed which improves the scale separation of the individual IMFs (Rehman et al. 2013; Mäteling and Schröder 2022). Two noise channels based on Gaussian distribution functions with a variance of 2% relative to the input data and zero mean are applied. The stopping criterion from Rehman et al. (2010) is used, which is based on the mean-square difference between two consecutive iterations normalized by the square of the previous sifting data. A bidimensional EMD formulation is used in the experimental FOV. In this version, the formulation of the envelope in the sifting process is based on a two-dimensional spline, i.e., a surface function. This approach differs from the formulation previously applied to in-cylinder flows, where combinations of one-dimensional spline functions in a row and column alignment are used, e.g. (Sadeghi et al. 2021; Ding et al. 2023, 2024). The bidimensional formulation can consider relations in both spatial directions, whereas the superposition of the one-dimensional approach can only approximate such relationships. The MEMD method has already been applied to turbulent boundary layer flow and PIV measurements of the shock buffet phenomenon in (Mäteling et al. 2023; Lagemann et al. 2024).

6 Results and Discussion

LES results obtained with different grid resolutions are presented. First, the ensemble averaged and individual cycle flow fields are compared with the experimental PIV measurements in the tumble plane. Subsequently, a mesh convergence study is presented, where the focus is on the evaluation of the single-grid estimator. Then, the influence of the number of cycles on integral and ensemble averaged velocity field data is discussed. Finally, results obtained by the MEMD of the velocity data in the tumble plane are presented. This includes a discussion of the scale separation and the advantage of the LF/HF decomposition for the validation of the numerical results and the CCV analysis.

6.1 Validation for the Ensemble Averaged Flow Field

First, a qualitative comparison of the LES results and experimental measurements data is presented in Figs. 4 and 5 for the ensemble mean velocity field in the tumble plane. The experimental ensemble mean data are based on PIV measurements of all 198 and 5 selected engine cycles. As summarized in Table 2, 5 consecutive cycles were used for the ensemble average of the simulation results, since the computational costs become excessively high, especially at the high grid resolution. The smaller number of cycles impacts the convergence of the ensemble averaged data such that no perfect match with the experimental data from 198 cycles can be expected. For all numerical simulation cases and for the lower number of experimental cycles small local velocity fluctuations are still visible in Figs. 4 and 5.

The instantaneous velocity data of one randomly selected cycle is displayed in Fig. 6 for the three different grid resolutions and the experimental PIV measurements. An excellent agreement in the turbulent instantaneous velocity field can be observed.

The simulation data show satisfactory agreement in comparison with the experimental data for the main tumble vortex and the regions with low velocity magnitude. In general, the velocity fields show similar flow structures at comparable locations for all crank angles and mesh resolutions. Some deviations occur at 90 [CAD], where a slightly larger velocity magnitude is predicted near the top boundary of the experimental FOV for all mesh resolutions. In this region, the two intake jets interact generating large turbulent fluctuations.

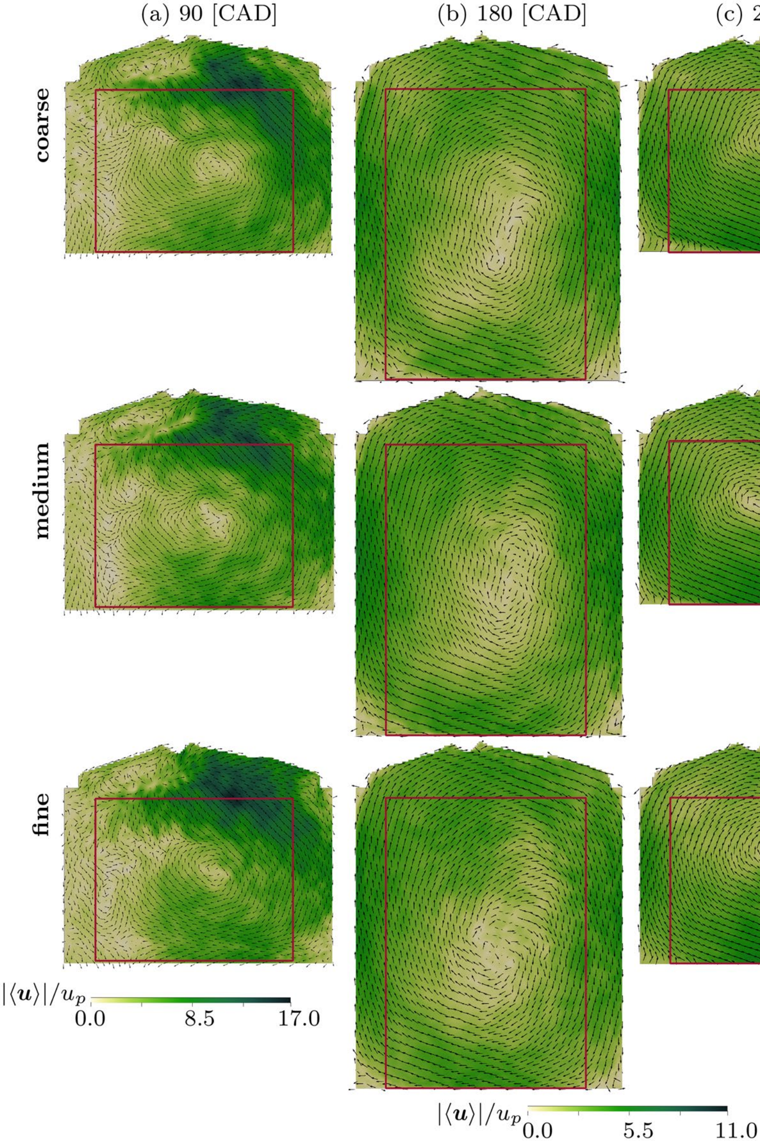

Fig. 4 Comparison of the LES results using different grid resolutions (*coarse*, *medium* and *fine*) for the ensemble averaged velocity field in the tumble plane. Results are shown for 90 [CAD] 180 [CAD] and 270 [CAD] The color map denotes the non-dimensional velocity magnitude and the arrows depict the orientation of the velocity vector. The red rectangle shown in the numerical results denotes the experimental FOV

Towards the left boundary of the experimental FOV, a region with low velocity magnitude and a highly fluctuating orientation of the velocity vector can be observed. In the tumble vortex core regions differences in the velocity vector orientation can be observed at BDC, i.e. 180 [CAD], and at 270 [CAD]. This indicates that the vortex core identification for the

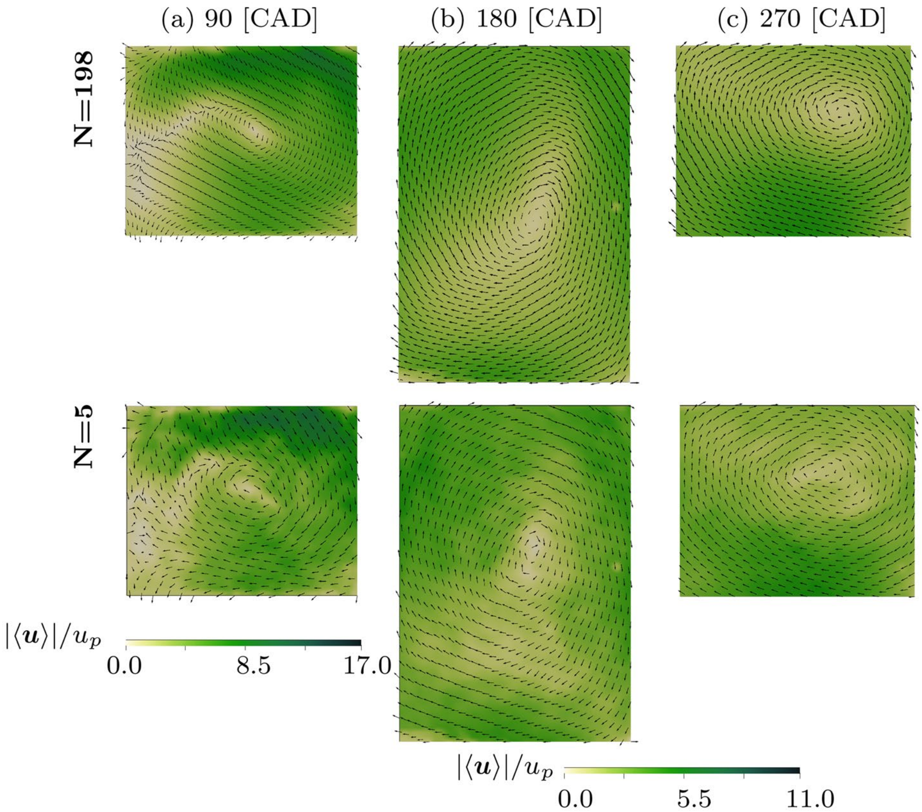

Fig. 5 Comparison of the ensemble averaged velocity data from PIV measurements with 5 and 198 cycles included in the average. Results are shown in the experimental FOV in the tumble plane for 90 [CAD] 180 [CAD] and 270 [CAD] The color map denotes the non-dimensional velocity magnitude and the arrows depict the orientation of the velocity vector

highly resolved LES data may yield varying results for individual cycles or ensemble mean data with the limited number of computed cycles. However, the differences in the velocity field are small for all numerical resolutions and the predicted velocity fields in the tumble plane agree reasonably well with the experimental data.

For a quantitative comparison of the ensemble mean velocity field, the relevance and magnitude indices (RI and MI from Eqs. (19) and (20) are computed. To compare the results with other validation studies only in-plane velocity components are considered for the RI and MI values. The temporal evolution of $\widetilde{RI}_{2D}$ and $\widetilde{MI}_{2D}$ for the *fine* resolution case is plotted in Fig. 7.

The relevance and magnitude index have similar values as the data reported in the literature and indicate good agreement of the simulation results with the experimental data. The largest deviations between the experimental and numerical data, i.e., the lowest RI and MI values, can be observed at the beginning of the intake stroke at around 90 [CAD]. At this stage, the high piston velocity reduces the in-cylinder pressure and creates high kinetic intake jets into the engine. After approx. 120 [CAD] a good match in the velocity orientation and magnitude is indicated by the high values for the RI (> 0.9) and MI (> 0.8). In general,

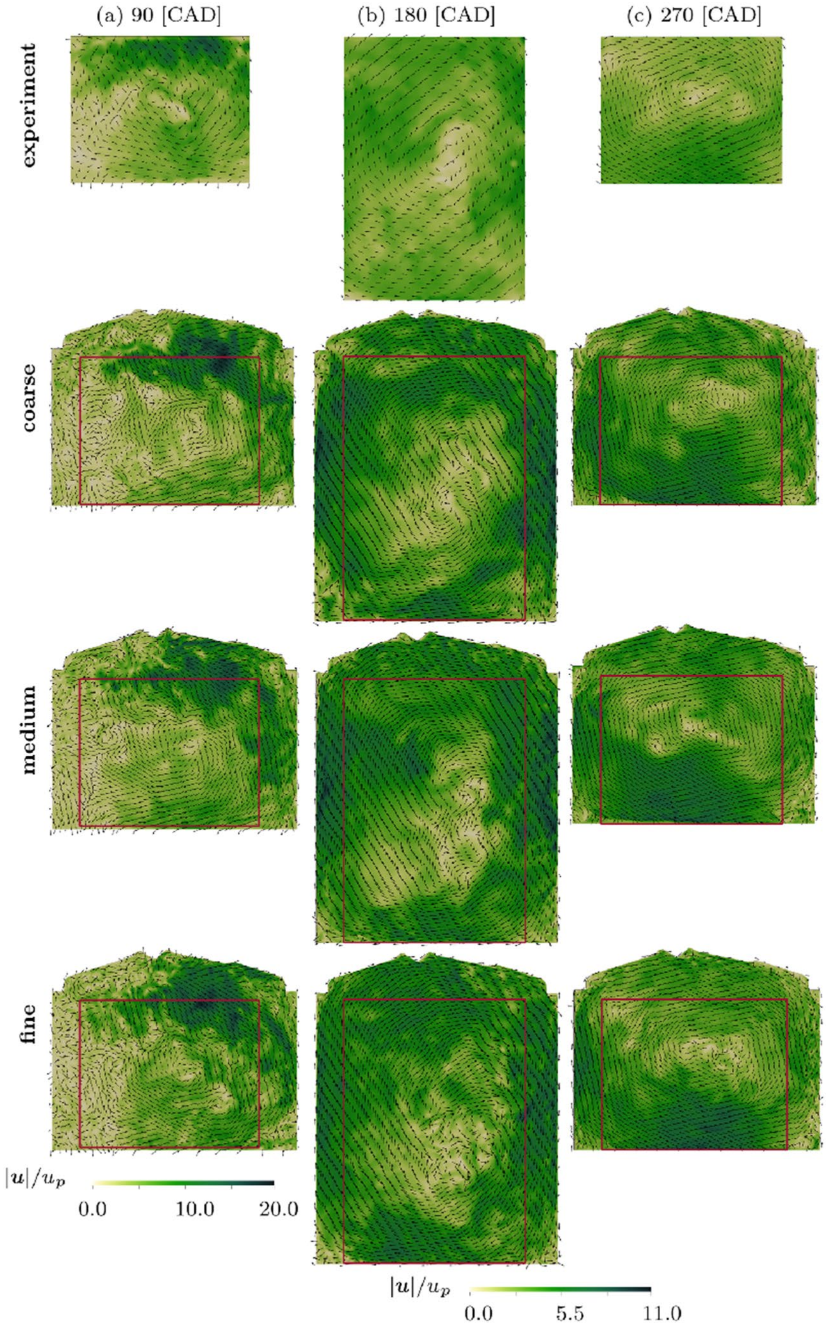

Fig. 6 Comparison of the instantaneous LES results using different grid resolutions (*coarse*, *medium* and *fine*) and the experimental PIV data in the tumble plane. Results are shown for 90 [CAD] 180 [CAD] and 270 [CAD] of a randomly selected cycle. The color map denotes the non-dimensional velocity magnitude and the arrows depict the orientation of the velocity vector. The red rectangle shown in the numerical results denotes the experimental FOV

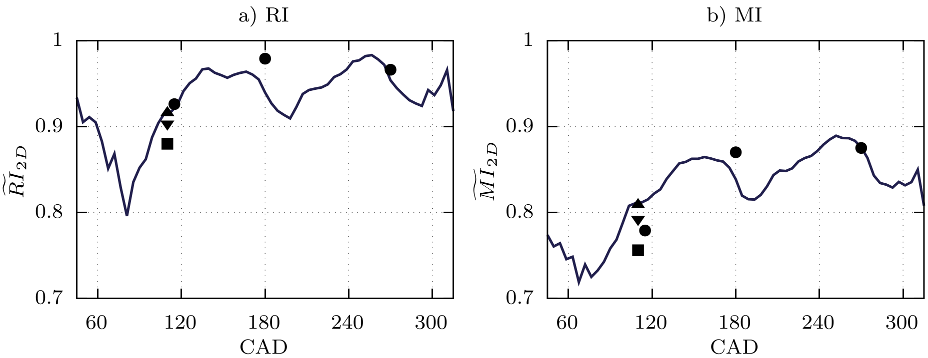

case	# of cells at BDC	# of cycles	symbol
fine mesh	$212 \cdot 10^6$	5	—
Barbato et al. [4]	$11 \cdot 10^6$	5	■
		10	▲
		25	▼
Krastev et al. [6]	$2 \cdot 10^6$	50	●

Fig. 7 Temporal evolution of the plane averaged relevance (**a**) and magnitude index (**b**) of the ensemble averaged in-plane velocity components for the *fine* mesh with 5 cycles and the experimental PIV data. Symbols for reference values from (Barbato et al. 2023) and (Krastev et al. 2019) are defined in the table

the RI value are larger values than the MI values. This indicates that the predicted velocity orientation compares better with the experimental data than the velocity magnitude.

In-plane RI and MI values from Krastev et al. (2019) and Barbato et al. (2023) for different engine configurations are included in Fig. 7. In comparison to the data from those studies, the present solution shows a slightly better agreement with the experimental results at 110 [CAD] even though a small number of cycles was used for the ensemble averaging. Note that the presented index values are based on the two in-plane velocity components since two-component PIV data were presented in (Barbato et al. 2023; Krastev et al. 2019).

When the third velocity component from the Stereo PIV data is taken into account, the values for the RI and MI are reduced on average by 0.021 and 0.025 for the *fine* resolution. The deviation increases slightly with decreasing mesh resolution, i.e., the average RI and MI values are lowered on average by 0.026 and 0.030 for the *medium* and *coarse* resolution. The RI and MI values were used primarily to compare the present results to the available data from other authors. Next, weighted indices will be used to compare instantaneous flow fields.

6.2 Validation for Instantaneous Flow Fields

The weighted indices WMI and WRI introduced by Willman et al. (2020), see Eq. (21), were shown to provide a better measure for the agreement of velocity fields, see also the appendix. The application to instantaneous flow fields allows for a comparison of individual cycle results from experimental and simulation data and the evaluation of cycle-to-cycle variations. The 5 cycles computed by LES are compared individually with all 198 experimental cycles. In the same way, 5 randomly selected experimental cycles are compared individually to all other experimental cycles.

All resulting plane averaged WRI and WMI values for the experimental data and the *fine* resolution setup are plotted in the cloud diagram in Fig. 8. Additionally, mean values are included. For the analysis three crank angles, i.e. 90 [CAD] 180 [CAD], and 270 [CAD], are selected, representing different flow regimes during the engine cycle. All resulting plane averaged WRI and WMI values for the experimental data and the *fine* resolution setup are plotted in the cloud diagram in Fig. 8. Additionally, mean values are included. For the analysis three crank angles, i.e. 90 [CAD] 180 [CAD], and 270 [CAD], are selected, representing different flow regimes during the engine cycle.

Note that lower WMI and WRI values generally indicate a better match between the two compared flow fields.

At 90 [CAD], when strong intake jets through the valve gap enter the cylinder volume, the largest differences between individual experimental cycles can be observed. This indicates large cycle-to-cycle fluctuations or stochastic turbulent fluctuations in the velocity field. The cloud diagram of the *fine* resolution cycles shows slightly larger WMI and WRI values where only a few data points overlap with the experimental variations. The average WRI and WMI values are 0.104 and 0.303 for the experimental cycles compared to 0.139 and 0.381 for the *fine* resolution setup. For the *medium* resolution setup the average indices are similar, but for the *coarse* resolution case they are significantly larger with average WRI and WMI values of 0.403 and 0.171. These values indicate differences in the instantaneous flow between the LES and experimental results. This could be caused by the PIV

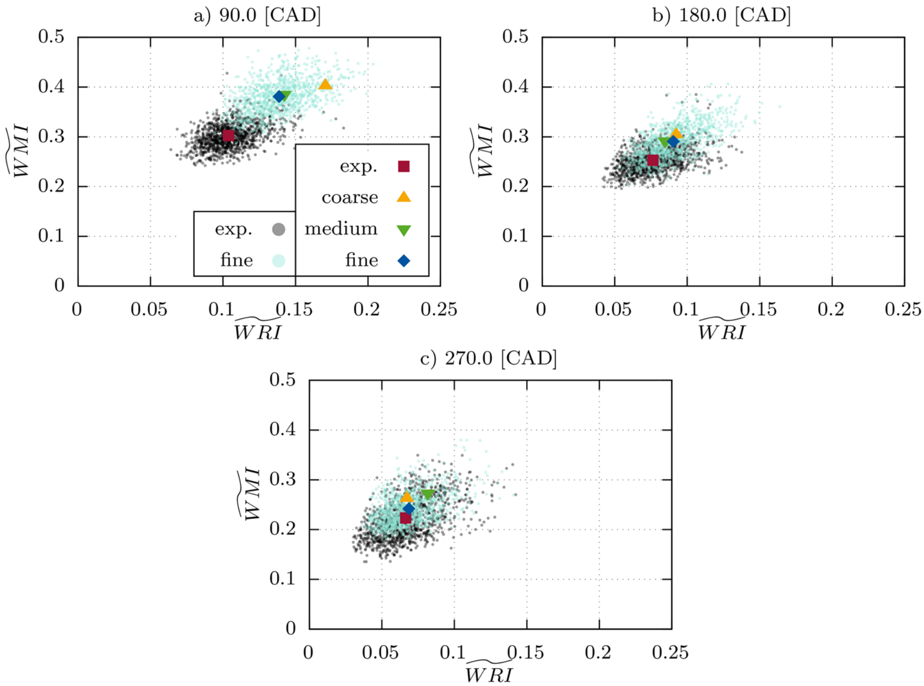

Fig. 8 Comparison of the weighted indices WRI and WMI for instantaneous velocity fields. The dots represent index values for individual cycles, while other symbols represent mean index values. The blue dots denote the index values for the 5 cycles predicted with the *fine* mesh resolution compared to all 198 experimental cycles. Indices from 5 randomly selected experimental cycles in comparison with all other experimental cycles are shown by the gray dots

measurement technique in which the finite frame-rate between snapshots filters turbulent velocity fluctuations at high frequency. Apart from that, uncertainties in the agreement of the numerical boundary conditions with the optical test engine case could play a role.

The EMD results, discussed in detail below show that the larger velocity scales agree better with the experimental data. The main deviations originate in the smaller turbulent scales, which could be underpredicted in the PIV results.

The differences in the instantaneous flow field diminish for increasing crank angle. At BDC, i.e.180 [CAD], variations between the different experimental cycles are smaller and a good overlap between the *fine* mesh and experimental WMI and WRI data points can be observed. The formation and evolution of the large scale tumble motion dominates the flow topology and is reproduced well by all mesh resolutions. This indicates that the cycles predicted by LES compare meaningful well with individual experimental engine cycles. For larger crank angles this tendency becomes more evident. At 270 [CAD] an excellent overlap between the *fine* and experimental cloud data points can be seen.

This extensive validation shows that a good match between the numerical simulation results and the PIV measurements in the tumble plane field of view has been achieved. Deviations in the flow field are limited to 60–100 [CAD]. In this time frame the intake jets and larger mean flow variations and stronger turbulent fluctuations exist. The best match with the experimental data could be achieved for the *fine* resolution setup, but with only slight differences compared to the *medium* resolution. The *coarse* mesh produces larger deviations during the intake stroke. The influence of the mesh resolution will be discussed further in the grid convergence study presented in the next section.

6.3 Grid Convergence Study

In the following, the influence of the grid resolution on the simulation results will be addressed. A first qualitative analysis is based on the volume rendered distribution of the specific kinetic energy $\langle e \rangle$ at 320 [CAD] shown in Fig. 9 for the *coarse* and *fine* mesh resolution ensemble averaged over 5 cycles.

Clearly, the *fine* setup shows higher kinetic energy values near the cylinder head compared to the *coarse* setup.

The integral mean of the kinetic energy of the *coarse* setup differs significantly from the two higher resolved cases towards the end of the compression stroke as illustrated in Fig. 10. The *medium* resolution setup on the other hand shows a good overlap with the *fine* resolution values with only a slight overprediction at the beginning of the compression stroke. The mean of the *coarse* cycles lies outside the cycle-to-cycle fluctuations of the *fine* setup for crank angles between 60 and 80 [CAD] and after 270 [CAD]. At 320 [CAD] the integral specific kinetic energy for the *coarse* resolution lies 16% below the value for the *fine* mesh case.

The deviation in kinetic energy is investigated further by means of the spatial distribution function of the ensemble mean kinetic energy $\langle e \rangle$ for the three mesh resolutions.

The ensemble mean flow field is computed by interpolating the individual cycle data to different grids with uniform refinement, based on the maximum grid resolution of the different setups. Spatial energy distribution functions are computed based on a binning process with a non-dimensional bin width of 0.07. The distribution functions at three selected crank angles are displayed in Fig. 11.

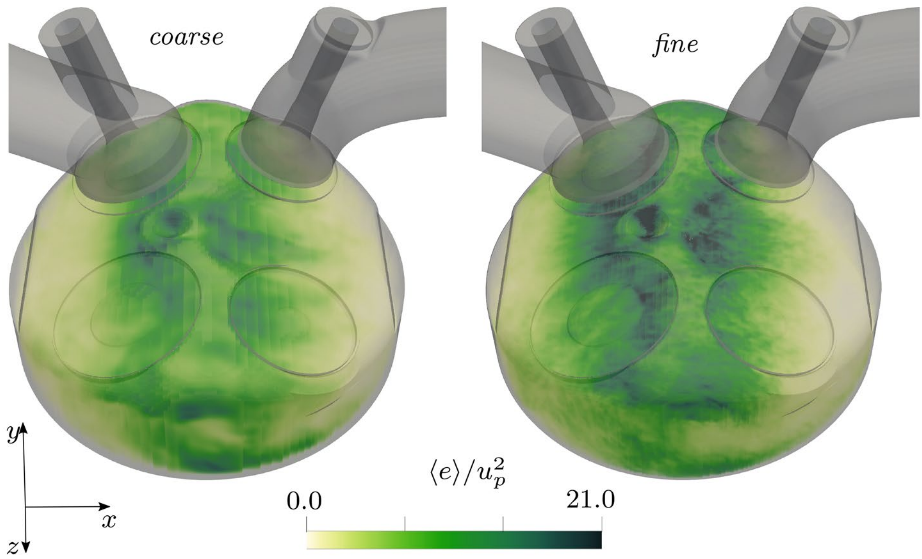

Fig. 9 Volume rendering of the non-dimensional specific kinetic energy $\langle e \rangle$ at 320 [CAD] for the *coarse* (left) and *fine* (right) mesh resolution. The volume rendering is created from ray marching algorithms based on the opacity of the specific kinetic energy

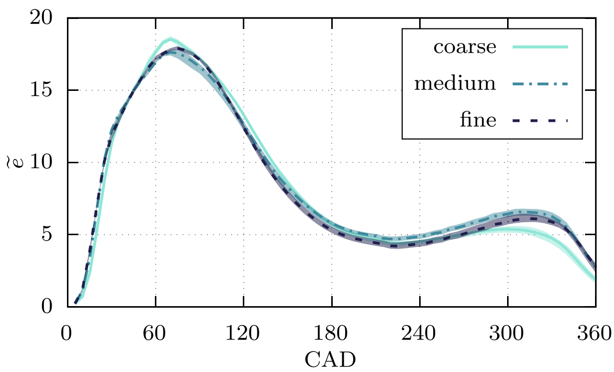

Fig. 10 Temporal evolution of the integral specific kinetic energy $\widetilde{e}$ in the cylinder for different grid resolutions. Lines indicate the cycle mean values, while shaded areas represent minimum and maximum values of the 5 investigated cycles

The comparison of the spatial energy distribution during the compression stroke reveals further differences between the *coarse* and higher resolved cases. Only minor differences in the spatial energy distribution curves can be observed during the intake stroke, e.g., at 70 [CAD]. For the *coarse* resolution a wider plateau emerges in the medium energy range, i.e., between 2–8 times the specific energy of the average piston velocity at 180 [CAD]. At this point the distribution of the *medium* resolution follows the general curve of the *fine* case except for a lower peak value.

These differences amplify during the compression stroke. At 320 [CAD], the *coarse* resolution distribution function has a narrower and significantly larger peak value in the lower velocity range. This is also reflected in the lower integral value, which represents the center of area of the distribution function. For this crank angle position the distribution function

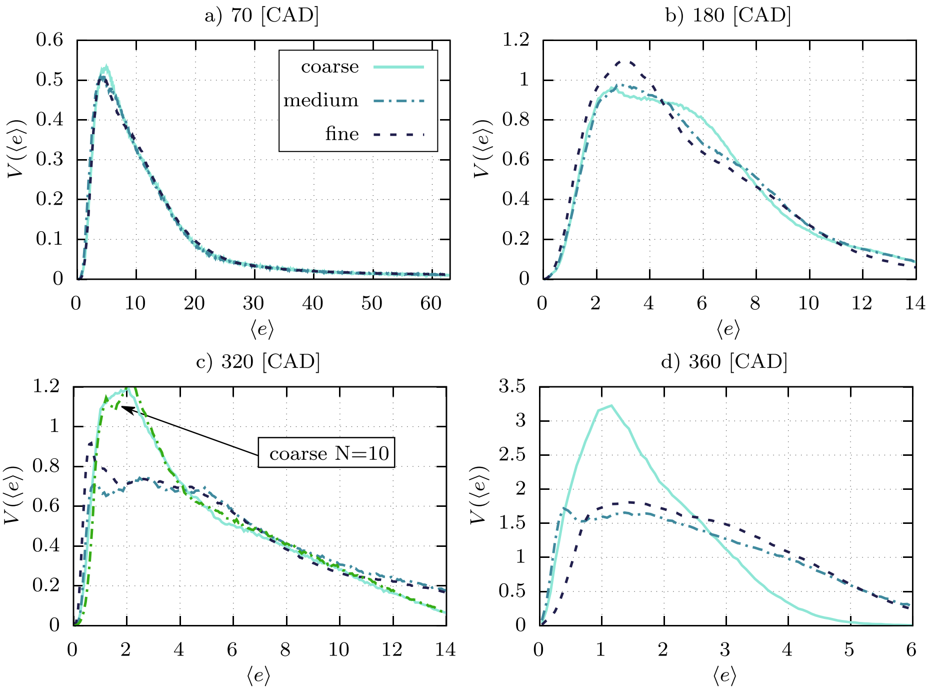

Fig. 11 Distribution function of the ensemble averaged kinetic energy $\langle e \rangle$ in the engine volume at 70 [CAD] (**a**), 180 [CAD] (**b**), 320 [CAD] (**c**), and 360 [CAD] (**d**) for the different grid resolutions for $N = 5$ cycles. The volume ratios are computed based on kinetic energy bins with a width of 0.07 and are a percentage of the in-cylinder volume. The energy range is selected such that the distribution displays 95% of the cylinder volume for the *fine* resolution cases. The green line in sub-figure c) represents the ensemble averaged kinetic energy for the *coarse* resolution with $N = 10$ cycles

of $\langle e \rangle$ for 10 *coarse* cycles is included in Fig. 11 c). This indicates a good convergence of the energy distribution function for 5 cycles and shows that the deviation from the higher resolved cases is not driven by the number of cycles in the averaging process. For the *medium* and *fine* resolution cases the energy distribution function shows a wider plateau and the kinetic energies appear to dissipate less throughout the compression stroke. At TDC the significance of the different energy distribution for the *coarse* resolution becomes obvious. This energy distribution function shows a stronger Gaussian like shape with a peak energy slightly above the energy of mean piston velocity. This could indicate an earlier turbulent breakup of the tumble vortex which would induce a Gaussian velocity distribution.

It can be concluded that the preservation of the kinetic energy of the tumble rotation can be influenced significantly for grid resolutions below the *medium* resolution case. This could be caused by the lower wall resolution of the *coarse* LES case. The deviation in the velocity flow field will influence the prediction of the early flame development which has a significant influence on the subsequent combustion behavior.

6.4 Single-Grid Estimator

The grid convergence is discussed further by means of the single-grid estimator $M(\boldsymbol{x}, \theta)$ defined in Eq. (26). This index has been applied to in-cylinder flow field analyses in previous studies to justify a LES grid resolution as sufficient or well resolved, see Barbato et al. (2023) or Baumann et al. (2014). They have deemed a resolution as *sufficient* for LES if the integral grid estimator $\widetilde{M}$ exceeds a threshold of 0.8. Furthermore, it is assumed that for a simulation to be deemed a DNS a value of at least 0.95 must be reached.

For all three numerical setups the integral single-grid estimator M is computed in the entire in-cylinder domain for the solution adaptive grid refinement of one exemplary cycle. The ensemble mean of the strain rate entities $\langle S_{i,j} \rangle$ are computed on a reference grid with uniform resolution and a cell length of 1.5 times the smallest cell length of the individual setups.

The evolution of $\widetilde{M}$ during the intake and compression stroke is displayed in Fig. 12. As expected a clear convergence towards 1 can be observed with increasing grid resolution indicating a convergence towards DNS results. Clearly, the proposed threshold of 0.8 for sufficient LES resolution is reached for all cases. Mean values during the intake and compression stroke are 9.5, 9.7 and 9.8 for the *coarse*, *medium*, and *fine* resolution cases. The lowest $\widetilde{M}$-values are obtained during the early intake phase when a strong shear flow is induced by low valve-cylinder-head gaps at high piston velocity.

However, great care should be applied to any conclusions drawn from these single-grid estimator values. The previous discussion has revealed significant differences in the flow field during the compression stroke of the *coarse* case compared to the higher resolution results. Note that the kinetic energy of the unresolved turbulent scales is approximated based on the strain rate tensor of the resolved velocity scales. However, the entities of the strain-rate tensor are a function of the cell width and appear to grow with increasing LES resolution. This means that the kinetic energy of the modeled turbulent scales is underestimated for coarse cell resolutions. If the Kolmogorov length scale would be available from DNS results, the turbulent kinetic energy could be estimated correctly. This would reduce the single-grid estimator value for a given LES resolution. Based on the presented grid convergence study the magnitude of the underestimated strain-rate tensor and the following overestimation of the grid quality index can be estimated. This is done for the *coarse* case by computing the grid estimator based on the strain-rate tensor of the *fine* resolution setup interpolated to the *coarse* grid. The resulting grid estimator for the *coarse* mesh resolution

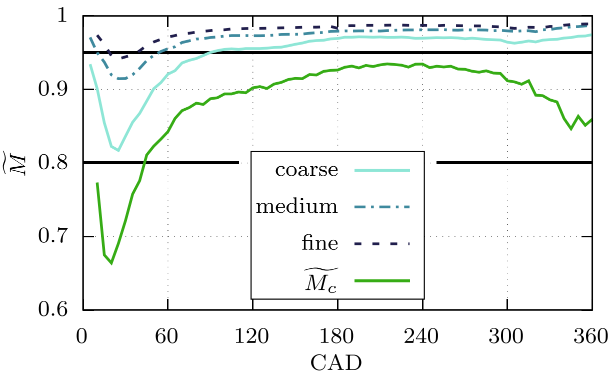

Fig. 12 Temporal evolution of the mean of the in-cylinder single-grid estimator $\widetilde{M}$ for the different resolution setups. $\widetilde{M_c}$ is based on the *coarse* resolution with the mean strain rate interpolated from the *fine* case onto the coarse refinement

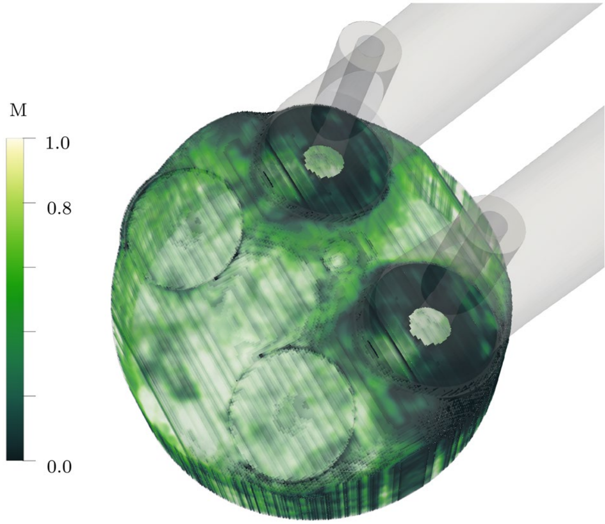

Fig. 13 Volume rendering of the single-grid estimator M_c for the *coarse* resolution setup at 50 [CAD] based on the strain rate tensor of the *fine* resolution

is denoted by $\widetilde{M_c}$ and shown in Fig. 12. In comparison with the original formulation $\widetilde{M_c}$ is lowered significantly during the entire intake and compression stroke. The temporal average drops from 0.95 to 0.88. Note that the *fine* resolution is not considered a DNS which indicates that the *true* grid estimator would be reduced further.

The spatial distribution of M_c in the engine is displayed in Fig. 13.

It can be seen that only a small percentage of the turbulent kinetic energy budget is resolved in the flow around the valves at 50 [CAD] for the *coarse* resolution. Recent studies indicate that turbulent eddies which form in this region during the inflow can influence the subsequent tumble development (Feng et al. 2023, 2024). Thus sufficient resolution of the turbulent eddies and their kinetic energy might influence the tumble motion and subsequent cycle-to-cycle variation.

Based on this discussion, the justification of LES grid resolutions using a threshold of $M = 0.8$ of the single-grid estimator can not be supported. The analysis has shown that a higher mesh refinement might be required even when M values lie above said threshold. It has been clearly shown that the value of $\widetilde{M}$ varies significantly in space and time during the intake- and compression stroke. Merely considering mean values can thus be misleading. Further, the computation of the single-grid estimator based on the strain-rate tensor on coarse resolutions does overestimate the value of $\widetilde{M}$. In brief, the current findings show that the single-grid estimator should be considered with care.

6.5 Influence of the Number of Cycles

In the following, the influence of the number of cycles N on the convergence of the ensemble averaging of various quantities is discussed. As a general rule, integrated quantities converge faster than point values.

6.5.1 Integral Quantities

First, the convergence of the volume integrated specific kinetic energy of the velocity fluctuations ($\widetilde{k}$) is discussed for the *medium* resolution setup.

The convergence of the ensemble averaging for $\widetilde{k}$ depends on the crank angle, i.e., the in-cylinder flow regime, as can be seen in Fig. 14 a). A larger number of cycles N is needed for $\widetilde{k}$ to converge at approx. 60 [CAD], where the intake jets or its interaction with the wall generate highly turbulent flow regions. $\widetilde{k}$ is underpredicted when a lower number of cycles is used. Outside the range of 30–110 [CAD], the averaged results using 5, 7 and 10 cycles are almost identical and appear to have reached convergence. The averaged results based on only 3 cycles follow the general trend, but during the entire intake and compression stroke, values are considerably lower. The cycle dependence is evaluated further by means of the convergence rate $\Delta\widetilde{k}_N$, i.e., the integral change in k with each additional cycle. $\Delta\widetilde{k}_N$ is computed at each crank angle Θ for different number of cycles N based on reference values from 10 cycles by

$$\Delta\widetilde{k}_N(\Theta) = \frac{|\widetilde{k}_{10}(\Theta) - \widetilde{k}_N(\Theta)|}{10 - N}.$$

This means that $\Delta\widetilde{k}_N$ represents the average change in $\widetilde{k}$ for N cycles, if one additional cycle is included in the ensemble average. $\Delta\widetilde{k}$ values and their mean of all crank angles are displayed in Fig. 14 b). Clearly, $\Delta\widetilde{k}$ diminishes for larger number of cycles and for $N \geq 5$ a difference of less than 0.02 remains with each additional cycle. This indicates a good convergence of integral flow quantities, in which spatial fluctuations average out due to the integration.

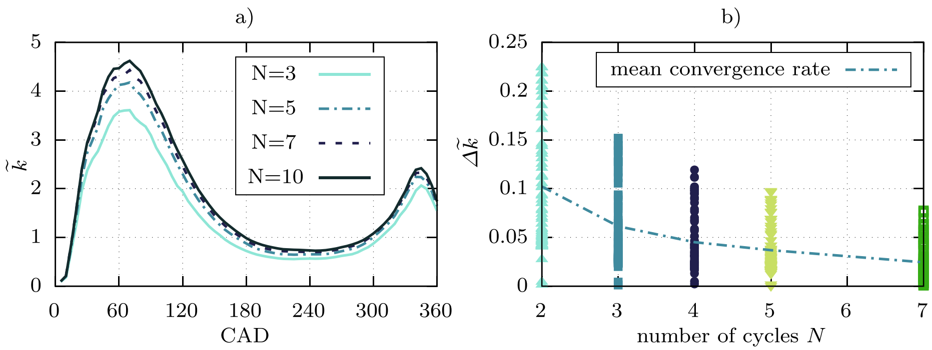

Fig. 14 (**a**) Temporal evolution of the turbulent kinetic energy $\widetilde{k}$ for using N cycles in the ensemble averaging for the *medium* resolution case. (**b**) Convergence rate of $\widetilde{k}$ with every additional cycle in comparison with the value obtained from 10 cycles for the *medium* resolution case. The point data denote individual crank angles and the line shows the linear mean convergence rate from all crank angles

6.5.2 Ensemble Mean Flow Field

Next, the influence of N on the weighted velocity indices WRI and WMI is considered. The indices are based on the agreement of the numerical ensemble averaged velocity with the experimental data. The velocity field is compared for all three mesh resolutions for 3 and 5 cycles and additionally for 7 and 10 cycles for the *medium* and *coarse* resolution. The results of the weighted vector field comparison with the experimental PIV data are displayed in Fig. 15.

When the number of cycles in the averaging process is increased from 3 to 5 the weighted index WRI decreases, indicating a better agreement with experimental data by 19.2%, 25.4% and 32.1% for the *coarse*, *medium* and *fine* resolution. Similarly, the WMI values are reduced by 7.5, 7.8 and 10.0%. This shows that WRI and WMI mean values indicate better agreement with the ensemble averaged experimental data when the number of cycles is increased. The cases with higher mesh resolution continue to improve further with increasing number of cycles. The vector alignment (WRI values) improves faster with more cycles than the vector magnitude (WMI values). This is the case even though the WMI_{ref} value exceeds the WRI_{ref} value by one order of magnitude.

Figure 15 also shows that with the increase from 5 to 10 cycles the improvement slows down and that WMI and WRI values tend to a limit value. In the *coarse* resolution case WMI is reduced by 13.7% and WRI by 32.0% when 10 cycles are used instead of 3. For 7 cycles WMI is already reduced by 10.7% and WRI by 28.3%.

The results also provide further insight into the grid convergence. By increasing the mesh resolution from *coarse* to *medium* WRI and WMI values are enhanced by 9.0% and 18.4% and moving further to *fine* even by 14.4% and 23.0% in the case of 5 cycles. This shows that for a fixed number of cycles an increase of mesh resolution will provide a better match with the experimental results.

However, note that 7 cycles of the *coarse* setup achieve nearly the same match with the experimental ensemble mean data as 3 cycles of the *fine* setup at only 2% of the computational cost. On the other hand, the results suggest that even for a high cycle number the settling values for WRI and WMI of the *coarse* case are higher than for the *fine* resolution with only 5 cycles.

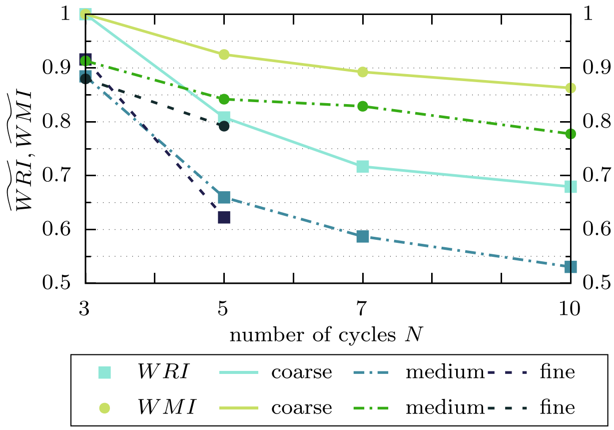

Fig. 15 Convergence of mean $\widetilde{WRI}$ (squares) and $\widetilde{WMI}$ (circles) values of the experimental FOV and the intake and compression stroke for the different grid resolution setups and different number of cycles N. The different resolution cases are represented by different line styles and the two different symbols represent the two indices. Values are non-dimensionalized by $WMI_{ref} = 0.237$ and $WRI_{ref} = 0.035$ which corresponds to the *coarse* resolution case with 3 cycles

It can be concluded that the improvement of the velocity indices tends to increase with increased grid resolution and that values appear to converge towards a better agreement for a large number of cycles. As the convergence rate differs between the resolutions especially for a low number of cycles, 3 averaging cycles are inadequate for a grid convergence study. However, 5 cycles appear sufficient for the prediction of relevant trends in the grid convergence and the estimation of the deviation compared to the experimental data.

Note that more cycles are required to obtain converged statistics of the fluctuating component of the Reynolds decomposition. Therefore, this analysis is only available for experimental data with a large number of cycles.

6.6 EMD Analysis

In the following, empirical mode decomposition (EMD) is applied to the in-cylinder flow to gain further insight on the large scale flow features for low number of cycles. First, the scale separation methodology is presented before results for the validation and the CCV analysis are discussed.

6.6.1 Scale Separation

The EMD decomposition in HF and LF scales is discussed quantitatively by means of Fig. 16 at 150 [CAD] for the *medium* resolution.

For this crank angle the velocity data is decomposed into 3 IMFs, which are combined in the HF part, such that the LF part consists only of the residual. It can be seen quantitatively that the tumble vortex, i.e., the rotational z-vorticity and the vortex core, is captured by the LF part in all cases. The LF component appears to have a better agreement with the experimental ensemble averaged data since it shows less smaller eddies and fluctuations. The velocity magnitude of the HF part is significantly lower than the magnitude of the LF part and the HF velocity vector shows a very chaotic behavior, especially for the numerical results. The largest HF velocities can be observed for individual numerical cycles. For the experimental data a significant magnitude in the HF velocity can be seen only in regions where larger inaccuracies are expected in the optical measurement technique and from the PIV reconstruction. This is the case where larger velocities enter (region A) or exit (region B) the FOV. Additionally, the pixel error in region C is intensified in the HF part and corrected in the LF part. The mode analysis reveals that these potential inaccuracies are captured in the first IMF of the experimental data.

The comparison between the EMD of the ensemble average based on 3 and 10 numerical cycles shows a decrease in the HF velocity magnitude with increasing number of cycles. This indicates that the numerical ensemble averaged input data contains small velocity scales which might disappear when further cycles are included in the average. Potentially, the HF velocity parts of the numerical mean could vanish for fully converged mean results. This aspect will be discussed further in the EMD validation analysis.

The LF component of the instantaneous velocity differs from the LF of the averaged data since individual cycles are subject to CCV also in the large length scale. This can be observed in the difference of the low and high LF velocity regions for the individual cycle in comparison with the LF ensemble mean. This issue will be discussed further in the EMD CCV analysis.

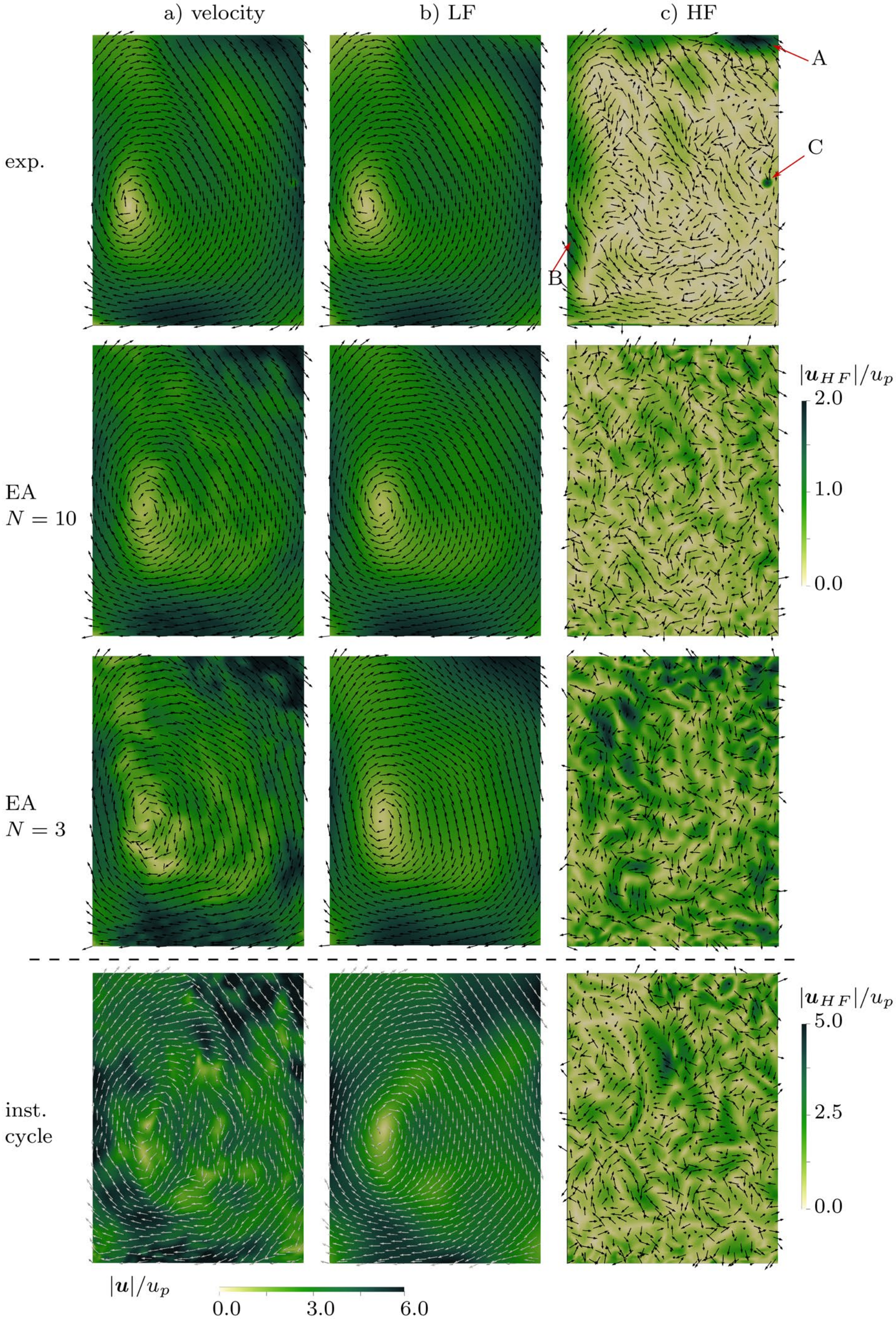

Fig. 16 EMD of the tumble plane velocity field at 150 [CAD] of the ensemble averaged PIV data (top row), of the ensemble averaged *medium* resolution case with 10 cycles (2nd row), with 3 cycles (3rd row) and of an instantaneous cycle (bottom row). The left column shows the velocity input data, center column the low frequency combination, and the right column the high frequency modes. Note that the color bar for the HF velocity differs from that of the other two velocities

First, the combination of the different IMFs and the residual in the HF and LF component will be discussed based on the EMD at 120 and 150 [CAD]. These instances are selected since different numbers of IMFs are extracted from the velocity data. To begin with, the longitudinal power spectral density (PSD) of the in-plane velocity components is presented for the ensemble averaged data in Fig. 17.

The PSD is computed by Welch's method (Welch 1967) for the LF and HF components and the original velocity data. The HF part reflects the velocity data with large wave numbers (κ), i.e., in the range of small length scales with a wavelength below $\frac{1}{5}$ of the bore diameter. For larger wave length the spectral energy appears to be captured mostly by the LF part. Differences in the experimental and numerical input velocity can be associated mainly with the HF part, whereas an excellent overlap can be observed in the LF component especially for the smallest wave numbers. At 150 [CAD] an additional mode is extracted and the last IMF is included in the LF part. The comparison between the two crank angles shows a similar spectral energy separation between the different contributions even though different numbers of modes are combined. A similar power spectral density behavior has been observed by Ding et al. (2023), who also showed that the two contributions are clearly decoupled.

The combination of the IMFs into the LF and HF part is based on an energy criterion similar to that of Sadeghi et al. (2021). For this approach the integral of the specific kinetic

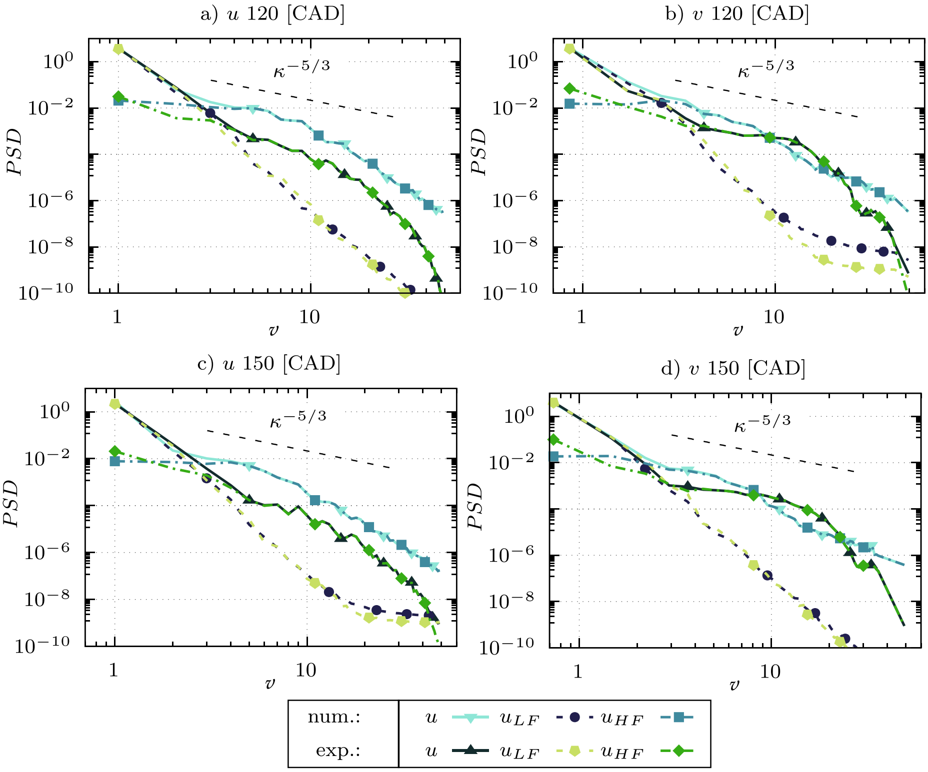

Fig. 17 Longitudinal PSD of the in-plane velocity components u (**a, c**) and v (**b, d**) of the ensemble averaged velocity field and their low and high frequency components based on the numerical (blue) and experimental (green) data for 120 [CAD] (**a, b**) and 150 [CAD] (**c, d**)

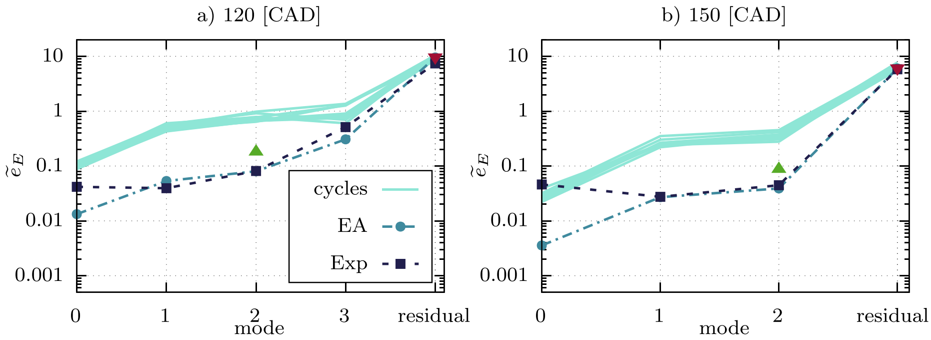

Fig. 18 Energy content of the different EMD modes and the residual at 120 [CAD] (**a**) and 150 [CAD] (**b**) The energy content of the mode combination is displayed by the two triangles, with the LF part in red and the HF in green. The cycle lines refer to the instantaneous data of the 10 individual cycles

energy of each IMF and the residual is computed for the ensemble averaged and instantaneous data. The results are displayed for the selected crank angles in Fig. 18.

Clearly the energy content of each mode increases with increasing mode number for the numerical data. The highest energy is contained in the residual. For the PIV data the energy of the first IMF differs from this trend. As shown before, large velocities can be observed in this first mode in regions where measurement inaccuracies are expected. Therefore, the energy content of the PIV data is disregarded in the mode separation.

Figure 18 further shows that the energy of the ensemble averaged data differs significantly, i.e., by approx. one order of magnitude, from that of the individual cycles in all first high frequency modes. This energy difference is selected as the mode separation criterion. This means that a mode is included in the LF combination if the energy content of the ensemble averaged data is similar to the instantaneous energy of the individual cycles, i.e., if the energy difference lies below the cycle fluctuations. Using this criterion, the HF energy content of the ensemble averaged data lies significantly below the energy of the LF combination. This is similar to the separation by Sadeghi et al. which is based purely on an energy threshold. However, for the investigated cases the energy of the last IMF of the instantaneous data can be on the same order of magnitude as the energy of the residual. This makes their definition of a specific energy threshold arbitrary. The proposed criterion makes use of the multivariate formulation which includes the ensemble mean and individual cycles in the EMD. The formulation has been applied successfully to all EMD analyses during the intake and compression stroke.

The physical meaningfulness of the selected mode separation can be shown by the analysis of the fluctuations in the LF and HF part by means of the Lumley invariant map (Choi and Lumley 2001) as introduced in the previous section. With the shared mode decomposition, the fluctuation stresses can be computed for the LF and HF velocity components from the instantaneous and ensemble averaged flow field date, e.g., $u\prime_{LF}(\theta_i) = u_{LF}(\theta_i) - u_{LF,EA}(\theta)$. Note that the EMD reconstruction maintains the ensemble averaged property, namely that the ensemble average of a velocity component of the individual cycles matches the velocity component obtained from the ensemble averaged input data. This is the case only for the same mode decomposition. The invariant maps for 120 and 150 [CAD] are displayed in Fig. 19.

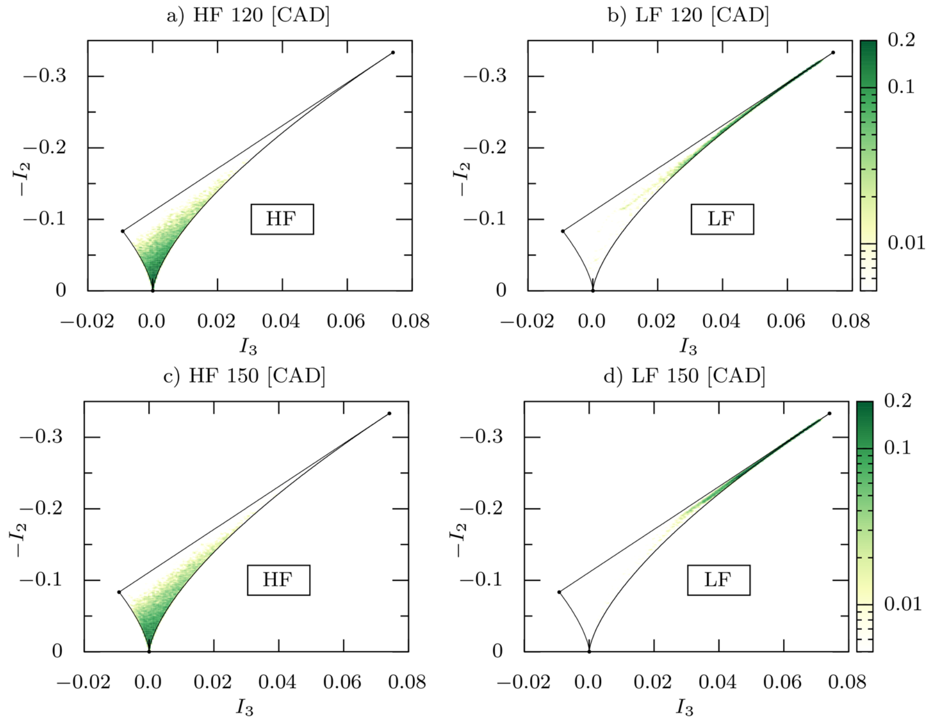

Fig. 19 Statistical analysis of the cycle fluctuations of the HF modes (**a, c**) and LF modes (**b, d**) at 120 [CAD] (**a, b**) and 150 [CAD] (**c, d**) of the EMD analysis for the *medium* mesh resolution setup with 10 cycles

Clearly the turbulent velocity statistics of the LF and HF velocity components differ significantly. For the HF modes fluctuations appear only near the 3D isotropic corner. On the other hand, fluctuations in the LF modes are concentrated in the corner associated with 1D turbulence and along the axis-symmetric expansion boundary. The analysis of the fluctuations of the entire velocity component for the experimental data showed only a 3D isotropic behavior. Additionally, the z-vorticity of the LF and HF components differs significantly. The z-vorticity of the HF component shows no predominant orientation and the integral is nearly zero. On the other hand, the z-vorticity of the LF component contains the vorticity of the tumble vortex of the input data. The clear difference in the velocity fluctuations and vorticity indicates a physically meaningful difference between the two velocity components and a meaningful separation in LF and HF part. This is especially the case for the presented mode separation, which delivers a reliable separation independent of the number of extracted modes for all investigated crank angles and mesh resolutions.

Note that the EMD is always based on the input data, which means that a different decomposition is obtained for different input data. For instance the decomposition of the experimental data shows small differences depending on the input data combination, i.e., depending on the included numerical data. However, the average difference in the LF integral energy for all numerical cases lies below 3% which underlines the physical consistency in the data and the scale separation.

Based on this separation the LF and HF components of the ensemble averaged flow and of the individual cycles will be discussed in the validation and CCV analysis.

6.6.2 EMD Validation Analysis

In a first step, the contribution of the HF component in the ensemble averaged data will be discussed for different number of cycles based on Fig. 20.

The integral energy of the HF component ($\widetilde{e}_{HF,E}$) appears to have a larger contribution only when the intake jets interact in the tumble plane and the ensemble average might not be fully converged. For 3 cycles, the HF kinetic energy contribution falls below 6% of the entire kinetic energy for CAD > 120. Additionally, the HF energy component is reduced when more cycles are taken into account. For 10 cycles, the HF kinetic energy contribution to the kinetic energy of the complete ensemble average falls below 2% after 120 [CAD]. This indicates that the LF component converges towards the ensemble average for larger numbers of cycles:

$$\langle u \rangle_{LF} \rightarrow \langle u \rangle \quad \wedge \quad \langle u \rangle_{HF} \rightarrow 0 \quad \forall N \rightarrow \infty$$

In other words, the high frequency energy component of the ensemble average velocity vanished for large N. For the experimental data with a large number of cycles a larger HF velocity and kinetic energy remain in regions with large uncertainties in the PIV measurements. Especially, this is the case when the high kinetic intake jets create large velocities at the boundary of the FOV. The LF component could be treated as a correction for PIV measurements, however, this analysis is beyond the scope of this numerical work. Thus, the complete experimentally measured velocity is used for the comparison with the numerical data.

The HF component in the ensemble averaged numerical data can be interpreted as turbulent or cycle fluctuations which remain in the mean value due to an insufficient number of cycles. Figure 17 also shows a higher kinetic energy content in the HF velocity components and a good match between the simulation results and the experimental velocity data in the LF components. This cycle convergence will be discussed further by comparing the LF component of the numerical ensemble average with the experimental data.

The comparison of the LF component of the ensemble averaged data with the PIV measurements is performed by the plane averaged WRI and WMI values as presented in the

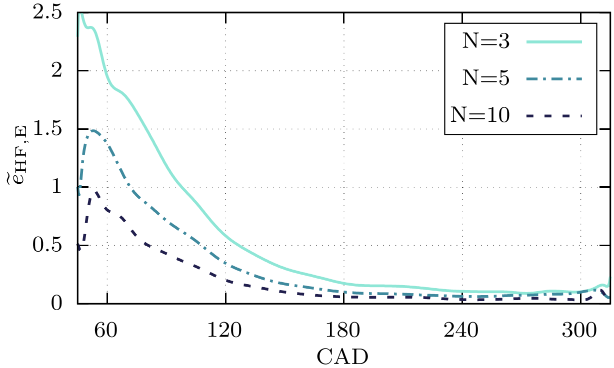

Fig. 20 Temporal evolution of the plane averaged specific kinetic energy of the HF component of the ensemble averaged velocity $\widetilde{e}_{HF,E}$ for different numbers of cycles for the *medium* resolution case

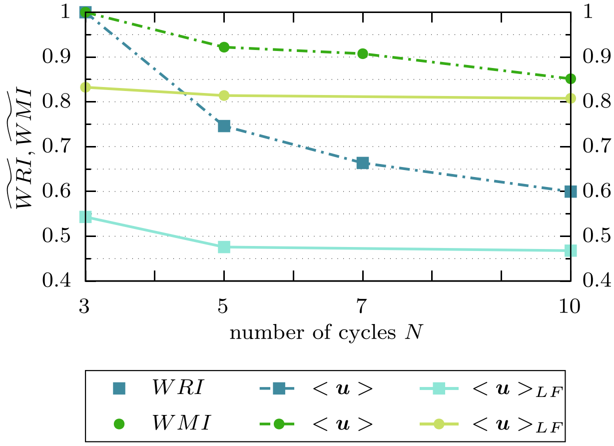

Fig. 21 Convergence of mean $\widetilde{WRI}$ (blue) and $\widetilde{WMI}$ (green) values in the experimental FOV during the intake and compression stroke for the *medium* grid resolution for different number of cycles N. The low-frequency component and the complete ensemble averaged velocity is compared with the complete experimental velocity component. Indices are non-dimensionalized by $WMI_{ref} = 0.217$ and $WRI_{ref} = 0.031$ which corresponds to the velocity data for the complete ensemble average with 3 cycles

previous LES validation section. The comparison is presented for 3, 5, and 10 cycles for the *medium* resolution in Fig. 21.

As stated before, an improved agreement with the experimental data can be observed with increasing number of cycles for the complete numerical ensemble average. The excellent match of the LF component which has been shown Fig. 16 is expressed by lower WMI and WRI values. For 10 cycles, mean $\widetilde{WMI}_{\mathrm{LF}}$ and $\widetilde{WRI}_{\mathrm{LF}}$ values of the LF velocity improve by 4.4% and 13.2% in comparison with the results obtained from the entire velocity. Additionally, the influence of the number of cycles is reduced and indices appear converged for more than three cycles. Most importantly, the indices obtained from the EMD appear to predict the WMI and WRI convergence with an increasing number of cycles. This means that the values obtained from the LF velocity component could be treated as the converged WMI and WRI values for a large number of cycles. Similar results have been obtained for all numerical cases. The overall best agreement has been obtained for the *fine* resolution case with 5 cycles with WMI and WRI values of 0.162 and 0.011.

Next, the LF component of the instantaneous velocity for individual cycles is compared to the experimental data. Again a WMI and WRI cloud diagram as presented in Fig. 8 of the validation section is used. The comparison for the LF component of the *fine* resolution case with the individual experimental cycles at 90 [CAD] is presented in Fig. 22.

Compared to the complete instantaneous velocity WMI and WRI values of the LF component are reduced by 47 and 14%. WMI_{LF} values lie in the same range as WMI values between experimental cycles. WRI_{LF} values even below WRI values between experimental cycles. This means that the deviation of the numerical results from individual experimental cycles lies below their cyclic variation. At the same time, large scale CCVs remain in the LF component.

Ding et al. (2023) suggest that large scale CCVs can be computed by the subtraction of the LF part from the entire ensemble averaged flow by

$$\Psi(\mathbf{x}, \theta_i)'_{CCV} = \langle \Psi(\mathbf{x}, \theta) \rangle - \Psi(\mathbf{x}, \theta_i)_{LF}.$$

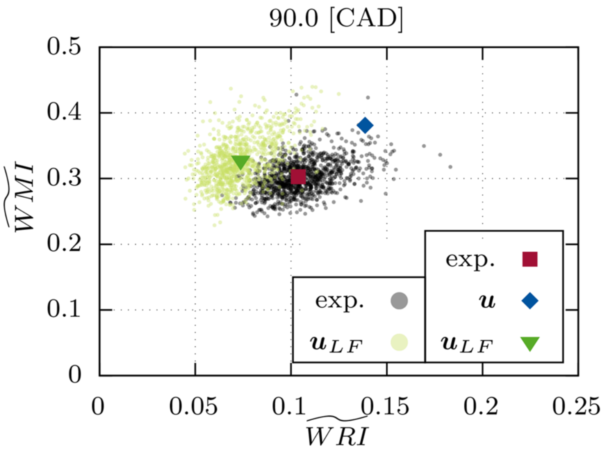

Fig. 22 Weighted comparison indices of instantaneous velocity fields. Individual $\widetilde{WMI}$ and $\widetilde{WRI}$ values are displayed by cycles and mean values by the angular symbols. The green shaded circles display the comparison between the low frequency velocity scale of the 5 *fine* mesh resolution cycles with all 198 experimental cycles. Indices from 5 randomly selected experimental cycles in comparison with all other experimental cycles are shown by the gray circles

for fully converged ensemble averaged data. In fact, this already implies that the converged ensemble mean data only consist of contributions in the low frequency range. This has been shown in this analysis.

In conclusion, the LF component shows an improved agreement with the experimental results for ensemble averaged and instantaneous data. The difference between the PIV results and the numerical data is largest in the HF component with short length and time scales. This could also be seen in the analysis of the PSD and could be caused by the higher spatial and temporal numerical resolution. The LF component of the ensemble averaged velocity from a low number of cycles can be used to estimate the converged mean flow. 5 cycles appear sufficient to obtain excellent $\widetilde{WRI}$ and $\widetilde{WMI}$ values in comparison with the experimental ensemble average with a large number of cycles.

6.6.3 EMD CCV Analysis

Variations in the large scale will be discussed further by means of the vorticity and the evolution of the tumble vortex core of the LF component for the *medium* resolution case with 10 cycles. The chosen setup provides a sufficiently fine mesh resolution and allows the simulation of a large number of cycles.

In a first qualitative analysis the velocity and LF velocity component of two selected cycles are considered at the beginning of the compression stroke and at 235 [CAD] in Fig. 23. White arrows have been added to highlight the differences in the velocity orientations and the instantaneous vortex cores are displayed by cycle specific colors.

The advantage of EMD and the presented scale separation becomes apparent by the comparison of the LF velocity component for two selected cycles. The strength and vortex core position of the tumble motion becomes apparent more easily. On the other hand, turbulent and other small scale fluctuations make a comparison between individual cycles more difficult. A distinctive low velocity region and a large flow deflection is visible in the center region for the LF component of cycle 11 at 180 [CAD]. Additionally an axially lower vortex core position is detected. For cycle 8, the vortex core is positioned further upwards. During the compression stroke the vortex core of cycle 11 is shifted further upwards and at 235 [CAD] it is positioned further towards the cylinder head compared to the vortex core from

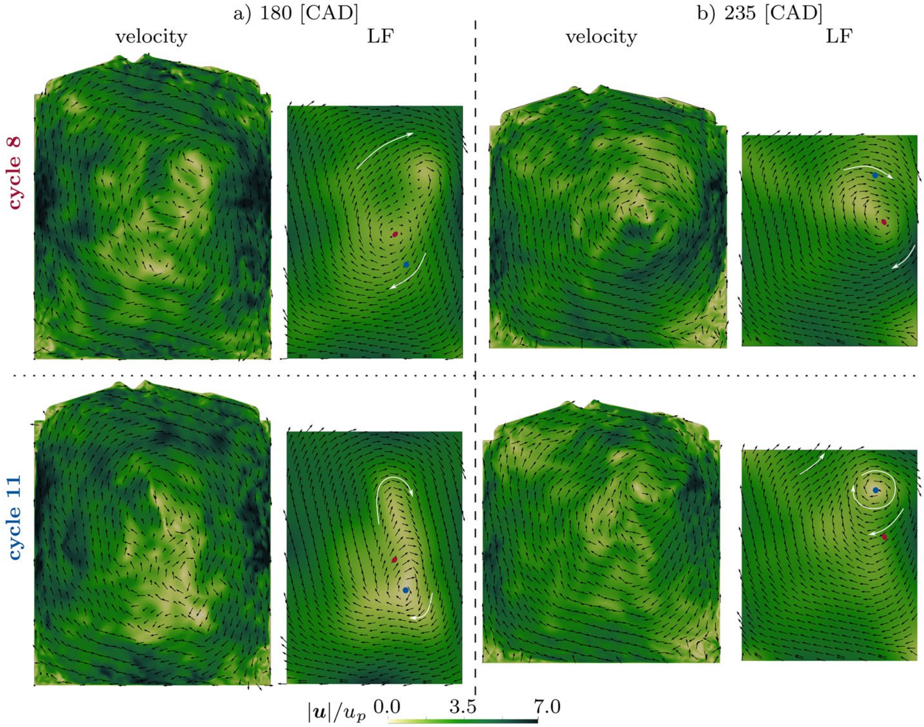

Fig. 23 Instantaneous velocity field at 180 [CAD] (left) and 235 [CAD] (right) for cycle 8 (top row) and cycle 11 (bottom row). The first and third column show the entire velocity data and the second and fourth column the large length scale (LF) component. The vortex core positions and the velocity orientation at selected positions are highlighted by red and blue points and white arrows

cycle 8. This implies significant CCVs in the evolution and pathway of the tumble vortex core at the beginning of the compression stroke for the two cycles. The temporal evolution of the vortex core is often seen as an intensifying element of CCVs (Feng et al. 2023) and will be investigated further.

First, the evolution of the vortex core of the ensemble averaged data from the experimental and the numerical results are compared in Fig. 24.

The formation of the tumble vortex begins during the first half of the intake stroke at an initially central position within the cylinder. During the intake, the core position shifts downwards like the piston direction. At the same time, the valve overflow of the intake jets shifts the vortex core further towards the intake side. During the compression stroke the vortex is shifted upwards by the piston motion and moves towards the exhaust side. At approx. 220 [CAD] the motion in the x-direction is reverted again and the vortex core moves towards the intake side. In comparison the vortex core position obtained from the LF component of the *medium* mesh resolution case agrees very well with the experimental data. Deviations are only visible in the y-position near BDC and in the x-position towards TDC. During these two phases the vortex core position is subject to significant CCVs and very sensitive in these directions. Figures 16 and 23 show that the extraction of the vortex core of the LF velocity part is unambiguous and no artifacts of small scale turbulent eddies

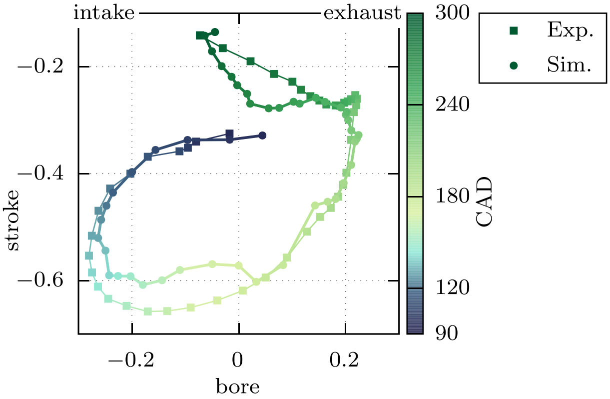

Fig. 24 Temporal evolution of the tumble vortex core position in the tumble plane of the low frequency part of the ensemble averaged velocity data for the *medium* mesh resolution cases with 10 cycles in comparison with experimental PIV data

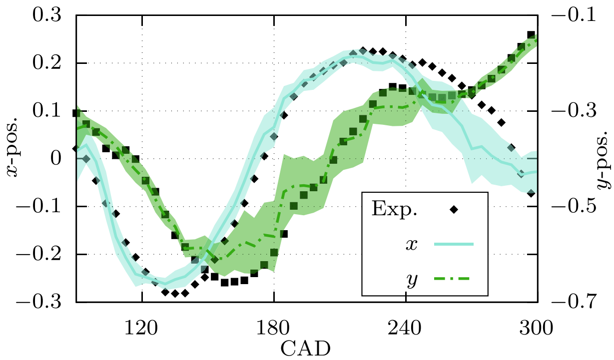

Fig. 25 Temporal evolution of the x- and y-position of the tumble vortex core in the tumble plane of the low frequency component of the instantaneous velocity of all individual cycles for the *medium* resolution. The line indicates the cycle mean, while the shaded areas represent the standard deviation from 10 cycles. Data points express the position of the experimental ensemble average

can be identified falsely. This simplifies the identification of the vortex core for individual cycles and enables further investigations of its cycle variation.

Such variations in tumble vortex core position are displayed in Fig. 25. The experimental results nearly always lie within the standard deviation of the CCV of the numerical results. Deviations remain only in the x-position for CAD between 250 and 280.

In the y-position significant cycle variations can be seen in the 150–250 [CAD] range, with a maximum variation of almost half the bore length and a standard deviation of at least 5% of the bore length in this crank-angle range. The impact of this cycle dependent behavior on the tumble strength is investigated in the following.

Figure 26 shows cycle variations in the integral z-vorticity of the LF velocity component of individual cycles.

Note that the integral vorticity of the HF velocity component is near zero for all cycles, thus the HF component can be neglected in the analysis of the tumble vorticity. Thus, the LF velocity represents the vorticity of the input data well and Fig. 26 shows a good match with the vorticity of the experimental ensemble averaged results. Large variations in the vorticity can be seen in the first half of the intake stroke (CAD $<$ 120) and at the end of the compression stroke (CAD $>$ 300). This indicates large scale CCVs during the interaction of the intake jets and the tumble breakup process. This has been observed also by Ding et al. (2023, 2024). Note that the integral vorticity in the tumble plane is also influenced by the spatial distribution of the rotational motion, which can shift in or out of the FOV. This

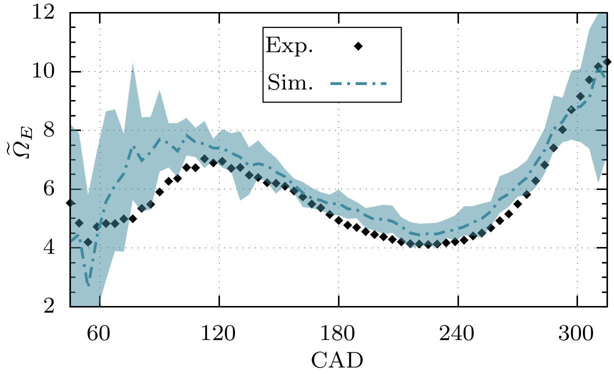

Fig. 26 Temporal evolution of the z-vorticity $\widetilde{\Omega}_E$ of the LF velocity component of the *medium* mesh resolution case in comparison with the experimental ensemble averaged data. The line and symbols indicate the cycle mean, while the shaded area represents minimum and maximum values from 10 cycles

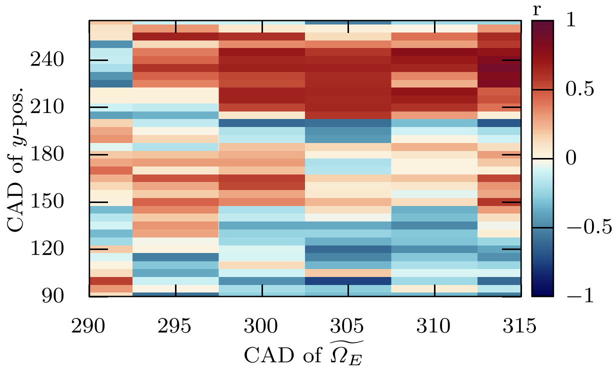

Fig. 27 Correlation of the y-position of the tumble vortex core and the z-vorticity $\widetilde{\Omega}_E$ of the LF component for the 10 cycles of the *medium* mesh resolution case

can be seen by comparison with z-vorticity in the entire engine, which reveals larger CCV towards the end of the compression stroke compared to the intake phase. In this case the vorticity variance at 350 [CAD] exceeds the maximum variance during the intake stroke by a factor of 1.4.

The tumble vorticity towards the end of the compression stroke is of particular interest since the vorticity near TDC has a significant influence on the fuel-air mixing for direct injection engines (Wegmann et al. 2023). A strong tumble motion is favorable since the increased vorticity can enhance fuel-air mixing before ignition. Therefore, the influence of the pathway of the tumble vortex core during the compression stroke on the vorticity near TDC and the tumble breakup is investigated for the different cycles.

In Fig. 27 the correlation between the vortex core y-position and the integral vorticity near TDC computed the Pearson correlation coefficient (see Eq.(29)) is shown.

A strong linear correlation can be observed between the vorticity towards the end of the observation window and the y-position at around 235 [CAD]. The largest correlation coefficient of 0.87 is found between the y-position at 235 [CAD] and the vorticity at 315 [CAD]. The correlation map shows a stable relationship with an average value of 0.65 in the crank angle range of 225 to 245 for the position and 300 to 315 for the z-vorticity.

The same trend can be observed when the y-position is correlated to the integral vorticity in the entire engine. The y-position between 235 and 245 [CAD] correlates linearly with the z-vorticity in the crank angle range of 305 to 345 by 0.67. The best correlation can observed between the y-position at 240 [CAD] and $\widetilde{\Omega}(340)$ with a correlation value of 0.88.

This means that the tumble vortex core position towards the cylinder head at around 235 [CAD] is favorable for a sustained tumble motion with a larger vorticity towards the end of the compression stroke. At the same time a sustained vortical flow correlates with an increase in kinetic energy towards TDC. The relationship between the pathway of the vortex core and the vorticity shows a larger linear correlation than the relationship between the vorticity itself. This means that the pathway might have a more direct influence on the TDC vorticity than the vorticity at an earlier stage of the intake and compression stroke.

This can be shown for the two selected cycles. For cycle 11, the vortex core has shifted further upwards towards the cylinder head compared to cycle 8 at 235 [CAD]. Cycle 11 shows a sustained tumble with a 64% larger vorticity in the tumble plane FOV at 315 [CAD]. The vorticity inside the entire engine is 13% larger, resulting in a 4% larger kinetic energy for cycle 11 compared to cycle 8. This could indicate that cycle 11 is more favorable for the fuel-air mixing towards the end of the compression stroke.

In conclusion, the extraction of the large scale tumble motion by EMD has proven a valuable tool for the analysis of CCV. This has been shown based on the pathway of the tumble vortex core during the compression stroke and the tumble vorticity. The z-vorticity is captured reliably by the LF velocity component, the vortex core extraction and the analysis of the tumble motion is simplified. The EMD based decomposition allows the computation of the LF velocity component of individual cycles for in-depth CCV analysis. A strong correlation between the y-position of the vortex core at approx. 235 [CAD] and the vorticity at the end of the compression stroke has been observed.

7 Conclusion

Implicit large-eddy simulations are conducted for the in-cylinder flow of an optical test-engine with three different numerical mesh resolutions. The comparison with stereoscopic PIV measurements in the tumble plane FOV has shown a satisfactory match in the velocity data with relevance indices in the range of 0.8 to 0.98 and magnitude indices in the range of 0.72 to 0.89 which is comparable or superior to relevant literature values. The ensemble mean flow and individual cycles are compared by the weighted relevance and magnitude index. The results indicate slightly larger velocities of the intake jet interaction but an excellent match at the end of the intake and during the compression stroke.

The grid convergence study reveals the influence of the mesh resolution on the flow field at the end of the compression stroke. Significant differences in the energy distribution and mean values are observed for the *coarse* mesh, caused by differences in the energy dissipation. At 320 [CAD] the integral specific kinetic energy for the *coarse* resolution lies 16% below the value for the *fine* resolution. The suitability of the single grid estimator for in-cylinder flow is discussed based on the numerical results obtained for the different resolutions. In brief, simply reaching a certain grid estimator threshold is not advised to justify a “satisfactory” grid resolution.

The influence of the number of cycles on the mean and fluctuating quantities is investigated. To better assess the cyclic variations and the ensemble-mean of the numerical data with limited number of cycles, a separation of the velocity scales by an EMD is applied.

The EMD approach simultaneously considers the velocity data of individual cycles, the ensemble average and experimental data. A novel scale separation methodology is introduced based on the energy of the ensemble averaged data and that of individual cycles. With this the number of IMFs which are grouped in the low and high frequency (LF and HF) component is data driven. The method is used to show that the LF velocity of the ensemble mean resembles the input ensemble mean data very well. The HF component decreases with increasing number of cycles. This indicates that the converged ensemble average can be estimated from a reduced number of cycles by the LF component. The method also allows the investigation of CCV in the large scale tumble motion, which can be obtained by the comparison of the LF components for different cycles. The sensitivity of the tumble vortex core and the impact of its pathway during the compression stroke is discussed. The correlation coefficient of 0.87 indicates a strong linear correlation between the y-position of the vortex core at approx. 235 [CAD] and the vorticity at 315 [CAD] towards the end of the compression stroke, has been observed.

Appendix A

Intake Boundary Condition

In the following the suitability of the prescribed characteristic boundary condition formulation for intake port applications is presented. In Fig. A1 the non-dimensional mass flow rate across the intake port two bore length upstream of the bore center is presented.

The results of the three numerical setups are compared to the incompressible mass flow rate based on the piston motion and cross-section area. A slight delay in form of a traveling wave is observed for the averaged simulation data of 5 cycles. However, due to the short stroke and low engine speed the intake flux does not choke and the curves match very well with the incompressible case. Consequently, a mass backflow can be observed for the

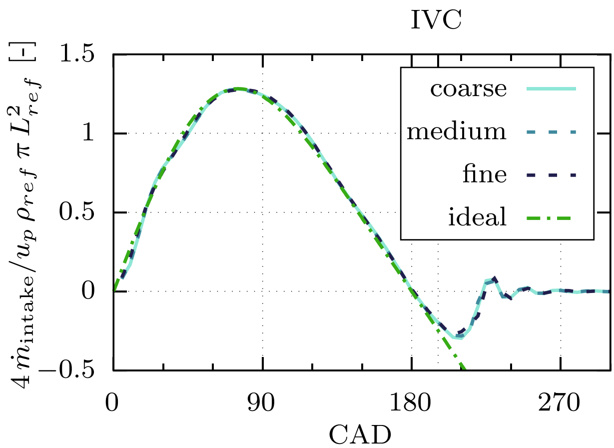

Fig. A1 Temporal evolution of the mass flow rate through the intake ports two bore length upstream of the cylinder. IVC denotes the nominal intake valve closing crank angle delayed intake valve closing (IVC) timing after BDC. After the valve closing the negative mass flow rate is reduced and levels off towards zero. The characteristic formulation is able to handle both local and temporal flow reversal and the subsequent near to zero mass flow rate across the boundary. No difference between the different grid resolutions can be observed and the lines of the simulation setups overlap. The same applies for the in-cylinder pressure curves. A strict convergence of the level-set representation of the engine geometry can be observed. The amount of trapped air in the cylinder is maintained by the strict mass conservative formulation of the finite-volume method as introduced in the numerical section.

Appendix B

Identification of the Tumble Vortex Core

Different stencil sizes S and threshold values of Γ have been evaluated based on their convergence towards a meaningful vortex core identification for the instantaneous flow fields of highly resolved LES simulations. The difficulties in the vortex core identification are displayed in Fig. B2 for two crank angles where multiple vortex cores can emerge.

It can be seen that multiple vortex cores are detected for small stencil sizes. Here it becomes difficult to distinguish between the vortex core motion during the cycle evolution and the false extraction of smaller turbulent eddies. Figure B2 shows a convergence of the vortex core to a single core position for stencil lengths corresponding to $1/4$ of the bore length and a threshold of 98% of the in-plane minimum Γ value. The analysis of all numerical cycles and resolutions has shown that this formulation yields a good detection and convergence for the tumble-vortex core position. In this context the stencil extent proposed by Falkenstein et al. (2017) has been adapted, but a different Γ detection threshold of $\Gamma = 0.98\Gamma_{\min}$ instead of their proposed value of $|\Gamma| = 0.8$ has been applied.

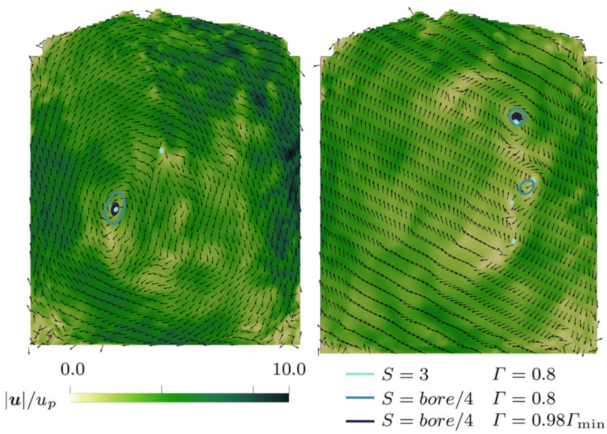

Fig. B2 Visualization of the convergence of the tumble vortex core position for different stencil sizes and Γ-thresholds at 150 [CAD] (left) and 210 [CAD] (right) for the instantaneous velocity flow field for the *medium* resolution setup

Appendix C

Low Velocity Sensitivity of RI and MI

In the RI and MI computation no distinction or weighting of different flow regions is applied. This means that slight deviations in the velocity orientation in regions with a low velocity magnitude (equivalent to low kinetic energy) can deteriorate the in-plane mean value significantly. This can be seen in the spatial distribution of the RI and MI values at BDC in Fig. C3, where low RI and MI values are concentrated in low velocity regions, i.e., near the tumble vortex core position.

However, the match of the orientation might not be as important for low velocity magnitudes as for higher magnitudes (Willman et al. 2020). To take this effect into account different weighting factor of the indices have been introduced (Barbato et al. 2023; Krastev et al. 2019; Willman et al. 2020). The specific weighting functions differ and no formulation seems to prevail. A velocity weighting based on the formulation of Willman et al. (2020) is adopted here (see Eq. (21)), as the formulation can be applied to instantaneous and ensemble averaged data and is not as strong as the weighting based on the kinetic energy from Krastev et al. (2019).

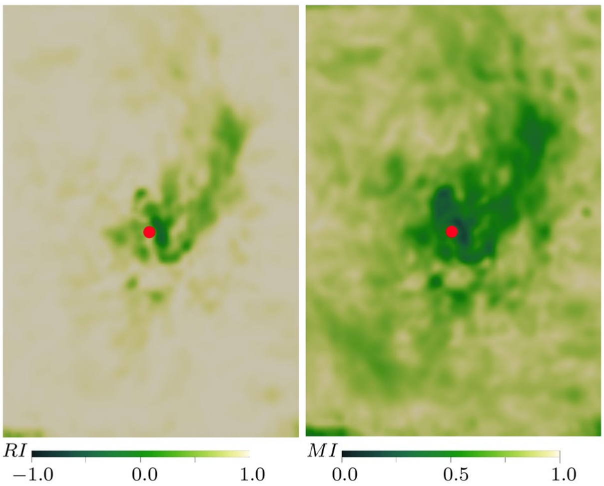

Fig. C3 Visualization of the RI and MI distribution computed for the comparison of the *fine* resolution case with the PIV data in the experimental FOV at 180 [CAD]. The presumed tumble vortex core is denoted by the red circle to display the center region with low velocity magnitude

Acknowledgements The authors gratefully acknowledge the funding by the Deutsche Forschungsgemeinschaft (DFG, German Research Foundation) under Germany's Excellence Strategy Cluster of Excellence 2186 "The Fuel Science Center"-ID: 390919832. The authors gratefully acknowledge the Gauss Centre for Supercomputing e.V. (www.gauss-centre.eu) for granting computing time on the GCS Supercomputer HAWK at Höchstleistungsrechenzentrum Stuttgart (www.hlrs.de). The authors gratefully acknowledge the Gauss Centre for Supercomputing e.V. (www.gauss-centre.eu) for funding this project by providing computing time on the GCS Supercomputer JUWELS at Jülich Supercomputing Centre (JSC). The authors gratefully acknowledge the computing time granted through JARA on the supercomputer CLAIX at RWTH Aachen.

Author Contribution Conceptualization: Wegmann, Lagemann, Meinke, Schröder; Methodology: Wegmann, Lagemann; Formal analysis and investigation: Wegmann; Writing—original draft preparation: Wegmann; Writing—review and editing: Wegmann, Lagemann, Meinke, Schröder; Funding acquisition: Meinke, Schröder; Resources: Wegmann, Meinke, Schröder; Supervision: Meinke, Schröder

Funding Open Access funding enabled and organized by Projekt DEAL. This project is funded by the Deutsche Forschungsgemeinschaft (DFG, German Research Foundation) under Germany's Excellence Strategy Cluster of Excellence 2186 "The Fuel Science Center" - ID: 390919832.

Data Availability A publicly available data repository has been provided (Wegmann 2025).

Code Availability The multi-physics solver m-AIA is available in an open-source software repository (2024).

Declarations

Ethics Approval and Consent to Participate The authors comply with the ethical standards.

Consent for Publication Informed consent was obtained from all authors before submitting this study.

Conflict of Interest The authors declare, that they have no conflicts of interest.

References

Barbato, A., Iacovano, C., Fontanesi, S.: Cold-flow investigation of the darmstadt engine with focus on statistical convergence: experimental and large eddy simulation analysis. Flow Turbul. Combust. **110**(1), 59–89 (2023). https://doi.org/10.1007/s10494-022-00370-6

Baum, E., Peterson, B., Böhm, B., Dreizler, A.: On the validation of LES applied to internal combustion engine flows: part 1: comprehensive experimental database. Flow Turbul. Combust. **92**(1–2), 269–297 (2014). https://doi.org/10.1007/s10494-013-9468-6

Baumann, M., Mare, F., Janicka, J.: On the validation of large eddy simulation applied to internal combustion engine flows part II: numerical analysis. Flow Turbul. Combust. **92**(1–2), 299–317 (2014). https://doi.org/10.1007/s10494-013-9472-x

Berger, M.J., Aftosmis, M.J., AllmarasS.R.: Progress towards a Cartesian cut-cell method for viscous compressible flow. AIAA Paper, 2012–1301 (2012)

Berger, S., Wegmann, T., Meinke, M., Schröder, W.: Large-eddy simulation study of biofuel injection in an optical direct injection engine. SAE Technical Paper **01**(2121) (2020)

Braun, M., Klaas, M., Schröder, W.: Influence of Miller cycles on engine air flow. SAE Int. J. Engines **11**(2), 161–178 (2018). https://doi.org/10.4271/03-11-02-0011

Braun, M., Klaas, M., Schröder, W.: Analysis of cyclic variation using time-resolved tomographic particle-image velocimetry. SAE Int. J. Adv. Curr. Prac. Mobility **3**(1), 113–136 (2020). https://doi.org/10.4271/2020-01-2021

Braun, M., Schröder, W., Klaas, M.: High-speed tomographic PIV measurements in a DISI engine. Exp Fluids **60**(9) (2019). https://doi.org/10.1007/s00348-019-2792-4

Buhl, S., Gleiss, F., Köhler, M., Hartmann, F., Messig, D., Brücker, C., Hasse, C.: A combined numerical and experimental study of the 3D tumble structure and piston boundary layer development during the intake stroke of a gasoline engine. Flow Turbul. Combust. **98**(2), 579–600 (2017). https://doi.org/10.1007/s10494-016-9754-1

Chen, H., Reuss, D.L., Sick, V.: On the use and interpretation of proper orthogonal decomposition of in-cylinder engine flows. Meas. Sci. Technol. **23**(8), 085302 (2012). https://doi.org/10.1088/0957-0233/23/8/085302

Choi, K.-S., Lumley, J.L.: The return to isotropy of homogeneous turbulence. J. Fluid Mech. **436**, 59–84 (2001). https://doi.org/10.1017/S002211200100386X

Ding, Z., Truffin, K., Jay, S.: Cause-and-effect chain analysis of combustion cyclic variability in a spark-ignition engine using large-eddy simulation, part I: from tumble compression to flame initiation. Combust. Flame. **267**(113566), (2024). https://doi.org/10.1016/j.combustflame.2024.113566

Ding, Z., Truffin, K., Jay, S., Schmidt, M., Foucher, F., Borée, J.: On the use of LES and 3D empirical mode decomposition for analyzing cycle-to-cycle variations of In-cylinder tumbling flow. Flow Turbul. Combust. **111**(1), 235–284 (2023). https://doi.org/10.1007/s10494-023-00405-6

Engelmann, L., Laichter, J., Wollny, P., Klein, M., Kaiser, S.A., Kempf, A.M.: Cyclic variations in the flame propagation in an spark-ignited engine: multi cycle large eddy simulation supported by imaging diagnostics. Flow Turbul. Combust. **110**(1), 91–104 (2023). https://doi.org/10.1007/s10494-022-00350-w

Falkenstein, T., Kang, S., Davidovic, M., Bode, M., Pitsch, H., Kamatsuchi, T., Nagao, J., Arima, T.: LES of internal combustion engine flows using Cartesian overset grids. Oil Gas Sci. Technol. - Rev. IFP Energies Nouvelles **72**(6), 36 (2017). https://doi.org/10.2516/ogst/2017026

Fang, X., Shen, L., Willman, C., Magnanon, R., Virelli, G., Davy, M.H., Stone, R.: Manifold reduction techniques for the comparison of crank angle-resolved particle image velocimetry (PIV) data and Reynolds-averaged Navier-Stokes (RANS) simulations in a spark ignition direct injection (SIDI) engine. Int. J. Engine Res. **23**(8), 1275–1294 (2022). https://doi.org/10.1177/14680874211013134

Feng, Y., Grill, M., Kulzer, A.: Numerical investigation on the cause-and-effect chain for cycle-to-cycle variation of direct-injection spark-ignition engine. SAE Technical Paper **24** (2023)

Feng, Y., Mirsch, N., Mir, D.I., Kulzer, A.C., Grill, M., Steeger, F., Blomberg, M., Pischinger, S.: Development of a 0D/1D model system for the cycle-to-cycle variation of high tumble spark ignition engines. SAE Technical Paper. **01**(2083) (2024)

Fogleman, M., Lumley, J., Rempfer, D., Haworth, D.: Application of the proper orthogonal decomposition to datasets of internal combustion engine flows. J. Turbul. **5**(23) (2004). https://doi.org/10.1088/1468-5248/5/1/023

Graftieaux, L., Michard, M., Grosjean, N.: Combining PIV, POD and vortex identification algorithms for the study of unsteady turbulent swirling flows. Meas. Sci. Technol. **12**(9), 1422–1429 (2001). https://doi.org/10.1088/0957-0233/12/9/307

Günther, C., Meinke, M., S.W.: A flexible level-set approach for tracking multiple interacting interfaces in embedded boundary methods. Comp. Fluids **102**, 182–202 (2014)

Heywood, J.B.: Internal combustion engine fundamentals, 2nd edn edn. McGraw-Hill Education, New York (2018)

Hirt, C., Amsden, A., Cook, J.: An arbitrary Lagrangian-Eulerian computing method for all flow speeds. J. Comput. Phys. **14**(3), 227–253 (1974). https://doi.org/10.1016/0021-9991(74)90051-5

Huang, N.E., Shen, Z., Long, S.R., Wu, M.C., Shih, H.H., Zheng, Q., Yen, N.C., Tung, C.C., Liu, H.H.: The empirical mode decomposition and the hilbert spectrum for nonlinear and non-stationary time series analysis. Proc. R. Soc. Lond. A. **454**(1971), 903–995 (1998). https://doi.org/10.1098/rspa.1998.0193

Huang, R.F., Huang, C.W., Chang, S.B., Yang, H.S., Lin, T.W., Hsu, W.Y.: Topological flow evolutions in cylinder of a motored engine during intake and compression strokes. J. Fluids Struct. **20**(1), 105–127 (2005). https://doi.org/10.1016/j.jfluidstructs.2004.09.002

Institute of Aerodynamics, RWTH Aachen University: m-AIA. Zenodo. **2024**(1) (2024). https://doi.org/10.5281/zenodo.13350586

Janas, P., Wlokas, I., Böhm, B., Kempf, A.: On the evolution of the flow field in a spark ignition engine. Flow Turbul. Combust. **98**(1), 237–264 (2017). https://doi.org/10.1007/s10494-016-9744-3

Krastev, V., D'Adamo, A., Rulli, F., Fontanesi, S.: Effects of the domain zonal decomposition on the hybrid URANS/LES modeling of the TCC-III motored engine flow. SAE Technical Paper **24** (2019)

Lagemann, E., Brunton, S.L., Schröder, W., Lagemann, C.: Towards extending the aircraft flight envelope by mitigating transonic airfoil buffet. Nat Commun. **15**(1) (2024). https://doi.org/10.1038/s41467-024-49361-3
Liu, K., Haworth, D.C.: Development and assessment of POD for analysis of turbulent flow in piston engines. SAE Technical Paper **01** (2011)
Lumley, J.L.: Computational modelling of turbulent flows. Adv. Appl. Mech. **18**, 123–175 (1978)
Mäteling, E., Albers, M., Schröder, W.: How spanwise travelling transversal surface waves change the near-wall flow. J. Fluid Mech. **957**, 30 (2023). https://doi.org/10.1017/jfm.2023.54
Mäteling, E., Schröder, W.: Analysis of spatiotemporal inner-outer large-scale interactions in turbulent channel flow by multivariate empirical mode decomposition. Phys. Rev. Fluids. **7.**(3) (2022). https://doi.org/10.1103/PhysRevFluids.7.034603
Meinke, M., Schneiders, L., Günther, C., Schröder, W.: A cut-cell method for sharp moving boundaries in Cartesian grids. Comp. Fluids **85**, 134–142 (2013)
Namazian, M., Heywood, J.B.: Flow in the piston-cylinder-ring crevices of a spark-ignition engine: effect on hydrocarbon emissions, efficiency and power. (1982). SAE Technical Paper
Niemöller, A., Schlottke-Lakemper, M., Meinke, M., Schröder, W.: Dynamic load balancing for direct-coupled multiphysics simulations. Comput. & Fluids **199**(104437), (2020). https://doi.org/10.1016/j.compfluid.2020.104437
Pirozzoli, S., Colonius, T.: Generalized characteristic relaxation boundary conditions for unsteady compressible flow simulations. J. Comput. Phys. **248**, 109–126 (2013). https://doi.org/10.1016/j.jcp.2013.04.021
Pogorelov, A., Schneiders, L., Meinke, M., Schröder, W.: An adaptive Cartesian mesh based method to simulate turbulent flows of multiple rotating surfaces. Flow Turbul. Combust. **100**(1), 19–38 (2018). https://doi.org/10.1007/s10494-017-9827-9
Poinsot, T.J., Lele, S.K.: Boundary conditions for direct simulations of compressible viscous flows. J. Comput. Phys. **101**(1), 104–129 (1992). https://doi.org/10.1016/0021-9991(92)90046-2
Pope, S.B.: Turbulent flows. Cambridge University Press, Cambridge (2000)
Rehman, N.U., Mandic, D.P.: Multivariate empirical mode decomposition. Proc. R. Soc. A. **466**(2117), 1291–1302 (2010). https://doi.org/10.1098/rspa.2009.0502
Rehman, N.U., Park, C., Huang, N.E., Mandic, D.P.: EMD via MEMD: multivariate noise-aided computation of standard EMD. Adv. Adapt. Data. Anal. **05**(2), 1350007 (2013). https://doi.org/10.1142/S1793536913500076
Rudy, D.H., Strikwerda, J.C.: A nonreflecting outflow boundary condition for subsonic navier-stokes calculations. J. Comput. Phys. **36**(1), 55–70 (1980). https://doi.org/10.1016/0021-9991(80)90174-6
Sadeghi, M., Truffin, K., Peterson, B., Böhm, B., Jay, S.: Development and application of bivariate 2D-EMD for the analysis of instantaneous flow structures and cycle-to-cycle variations of In-cylinder flow. Flow Turbul. Combust. **106**(1), 231–259 (2021). https://doi.org/10.1007/s10494-020-00197-z
Sakowitz, A., Mihaescu, M., Fuchs, L.: Flow decomposition methods applied to the flow in an IC engine manifold. Appl. Therm. Eng. **65**(1–2), 57–65 (2014). https://doi.org/10.1016/j.applthermaleng.2013.12.082
Schneiders, L., Günther, C., Meinke, M., Schröder, W.: An efficient conservative cut-cell method for rigid bodies interacting with viscous compressible flows. J. Comput. Phys. **311**, 62–86 (2016). https://doi.org/10.1016/j.jcp.2016.01.026
Schneiders, L., Hartmann, D., Meinke, M., Schröder, W.: An accurate moving boundary formulation in cut-cell methods. J. Comput. Phys. **235**, 786–809 (2013). https://doi.org/10.1016/j.jcp.2012.09.038
Selle, L., Nicoud, F., Poinsot, T.: Actual impedance of nonreflecting boundary conditions: implications for computation of resonators. Aiaa. J. **42**(5), 958–964 (2004). https://doi.org/10.2514/1.1883
Smagorinsky, J.: General circulation experiments with the primitive equations. Mon. Wea. Rev. **91**(3), 99–164 (1963)
Stiehl, R., Bode, J., Schorr, J., Krüger, C., Dreizler, A., Böhm, B.: Influence of intake geometry variations on in-cylinder flow and flow–spray interactions in a stratified direct-injection spark-ignition engine captured by time-resolved particle image velocimetry. Int. J. Engine Res. **17**(9), 983–997 (2016). https://doi.org/10.1177/1468087416633541
Sutherland, W.: The viscosity of gases and molecular forces. Lond., Edinburgh Dublin Phil. Mag. J. Sci. **36**(223), 507–531 (1893). https://doi.org/10.1080/14786449308620508
Tropea, C., Yarin, A., Foss, J.: Springer handbook of experimental fluid mechanics. Springer, Berlin (2007)
Udaykumar, H.S., Mittal, R., Rampunggoon, P., Khanna, A.: A sharp interface cartesian grid method for simulating flows with complex moving boundaries. J. Comput. Phys. **174**(1), 345–380 (2001). https://doi.org/10.1006/jcph.2001.6916
Wegmann, T.: Dataset for an EMD analysis of the flow field in an internal combustion engine. Zenodo. **2026**(1) (2025). https://doi.org/10.5281/zenodo.19479908

Wegmann, T., Meinke, M., Fleischmann, M., Pischinger, S., Schröder, W.: Numerical analysis of mixing of bio-hybrid fuels in a direct injection engine with a pre-chamber ignition system. SAE Technical Paper **01**(2619) (2024)

Wegmann, T., Meinke, M., Schröder, W.: Numerical analyses of spray penetration and evaporation in a direct injection engine. SAE Technical Paper **01**(310) (2023)

Wegmann, T., Niemöller, A., Meinke, M., Schröder, W.: Parallel Eulerian-Lagrangian coupling method on hierarchical meshes. J. Comput. Phys. **521**(113509), 113509 (2025). https://doi.org/10.1016/j.jcp.2024.113509

Welch, P.: The use of the fast fourier transform for the estimation of power spectra: a method based on time averaging over short, modified periodograms. IEEE Trans. Audio Electroacoust. **15**(2), 70–73 (1967). https://doi.org/10.1109/TAU.1967.1161901

White, F.M.: Viscous fluid flow, 3rd edition edn. McGraw-Hill, Boston (2006)

Willman, C., Scott, B., Stone, R., Richardson, D.: Quantitative metrics for comparison of in-cylinder velocity fields using particle image velocimetry. Exp. Fluids **61**(2) (2020). https://doi.org/10.1007/s00348-020-2897-9

Zentgraf, F., Baum, E., Böhm, B., Dreizler, A., Peterson, B.: On the turbulent flow in piston engines: coupling of statistical theory quantities and instantaneous turbulence. Phys. Fluids **28**(4) (2016). https://doi.org/10.1063/1.4945785

Zhao, F., Liu, M., Ge, P., Hung, D.L.S., Li, X., Xu, M., Yang, X., Idicheria, C.: Multi-plane time-resolved particle image velocimetry (PIV) flow field measurements in an optical spark-ignition direct-injection (SIDI) engine for large-eddy simulation (LES) model validations. Oil Gas Sci. Technol. – Rev. IFP Energies Nouvelles **74**, 52 (2019). https://doi.org/10.2516/ogst/2019022

Zhao, J.X., Lee, C.F.: Modeling of blow-by in a small-bore high-speed direct-injection optically accessible diesel engine. SAE Technical Paper. **01** (2006)

Authors and Affiliations

Tim Wegmann[1] · Esther Lagemann[2] · Matthias Meinke[1] · Wolfgang Schröder[1,3]

✉ Tim Wegmann
t.wegmann@aia.rwth-aachen.de

Esther Lagemann
e.maeteling@aia.rwth-aachen.de

Matthias Meinke
m.meinke@aia.rwth-aachen.de

Wolfgang Schröder
office@aia.rwth-aachen.de

1 Institute of Aerodynamics and Chair of Fluid Mechanics, RWTH Aachen University, Wüllnerstr. 5a, 52062 Aachen, Germany

2 AI Institute in Dynamic Systems, Department of Mechanical Engineering, University of Washington, Seattle, WA 98195, USA

3 Jülich Aachen Research Alliance Center for Simulation and Data Science, RWTH Aachen University and Forschungszentrum Jülich, Seffenter Weg 23, 52074 Aachen, Germany